

Cross-mode Stabilized Stochastic Shallow Water Systems Using Stochastic Finite Element Methods

Chen Chen*, Clint Dawson, Eirik Valseth

Oden Institute for Computational Engineering and Sciences, The University of Texas at Austin. 201 E. 24th St. Stop C0200, Austin, Texas 78712

Abstract

The development of surrogate models to study uncertainties in hydrologic systems requires significant effort in the development of sampling strategies and forward model simulations. Furthermore, in applications where prediction time is critical, such as prediction of hurricane storm surge, the predictions of system response and uncertainties can be required within short time frames. Here, we develop an efficient stochastic shallow water model to address these issues. To discretize the physical and probability spaces we use a Stochastic Galerkin method and a Incremental Pressure Correction scheme to advance the solution in time. To overcome discrete stability issues, we propose cross-mode stabilization methods which employs existing stabilization methods in the probability space by adding stabilization terms to every stochastic mode in a modes-coupled way. We extensively verify the developed method for both idealized shallow water test cases and hindcasting of past hurricanes. We subsequently use the developed and verified method to perform a comprehensive statistical analysis of the established shallow water surrogate models. Finally, we propose a predictor for hurricane storm surge under uncertain wind drag coefficients and demonstrate its effectivity for Hurricanes Ike and Harvey.

Keywords: Uncertainty Quantification, Stochastic Galerkin, Incremental Pressure Correction, Shallow Water Equations, Cross-mode stabilization

2000 MSC: 65M60, 35Q35, 35R60

*Corresponding author

Email addresses: chen636489@utexas.edu (Chen Chen), Clint.Dawson@austin.utexas.edu (Clint Dawson), Eirik@utexas.edu (Eirik Valseth)

1. Introduction

Over the past few decades, uncertainties of computational models have been recognized and studied by researchers from a wide range of fields, e.g., environmental engineering [1, 2, 3], geosciences [4, 5, 6], and in coastal engineering [7, 8]. A series of sampling-based non-intrusive methods [9, 10, 11] have been developed to quantify the uncertainty of certain computational models. The advantage of such methods is that the deterministic model can remain as-is and be considered as a black-box. However, to formulate a surrogate over any quantity of interest of a model, these methods usually require sample outputs which are obtained from a significant number of deterministic model computations. Thus, collecting the sample outputs requires significant computational resources and can therefore take long periods of time to establish. In time sensitive forecast models, such as storm surge models, it is important to develop fast uncertainty quantification. Hence, in this work, we propose a novel model called the Stochastic Shallow Water Model (SSWM) to forecast and quantify the associated uncertainties of storm surge.

In this model, we apply the Spectral Stochastic Finite Element Method (SSFEM) to achieve real time uncertainty forecasts for two dimensional shallow water equations (SWE). The introduction of uncertainties into the SWE leads to a numerical stability issue because the SSFEM introduces a modes-coupled stochastic hyperbolic system which is known to be unstable due to the possible formulation of shocks. To our knowledge, there exists no consistent stabilization method for the SWE stochastic hyperbolic system. To overcome this stability issue, we propose and implement a series of stabilization methods. We subsequently verify and validate the resulting SSWM surrogates by using well known numerical test cases for verification and two historic hurricane events in the Gulf of Mexico for validation.

Statistical analysis of uncertain model outputs via non-intrusive methods has been the subject of significant research [12, 13, 14, 15, 16] and allows users to obtain consistent mean and variance information. Higher order statistical moments, reliable probability density functions (PDFs), as well as the support of the output random process are more difficult to ascertain. This difficulty is exaggerated further when the information is needed in a short time frame in real-time forecasting systems. The support of the output random variable (i.e., the range of random variable in which its value falls) is of great importance to the reliability

analysis in coastal engineering [17]. From the developed SSWM and its surrogates, higher order moments, PDFs, and random variable support are readily available for statistical analysis.

In the following, we introduce and comprehensively verify and validate a new SSWM. First, in Section 2 we introduce the SSWM with a particular focus on the novel stabilization methodology developed. In Section 3, we verify and validate the SSWM. Next, in Section 4, we perform statistical analyses of the SSWM surrogate responses. In Section 5, we apply the SSWM to predict hurricane storm surge under uncertain wind drag parameters. Finally, in Section 6, we draw conclusions and discuss future research directions.

2. The Stochastic Shallow Water Model

2.1. Mathematical Formulation

Our SSWM is based on two-dimensional deterministic shallow water equations (SWEs) under standard assumptions of incompressible isotropic flow with constant density and kinematic viscosity. We also assume a hydrostatic pressure distribution and a long-wave condition so vertical fluid motion is negligible. We therefore consider the two-dimensional deterministic SWEs as follows [18, 19]:

$$\begin{aligned} \frac{\partial \eta}{\partial t} + \nabla \cdot (H\mathbf{u}) &= 0 \text{ in } \Omega, \\ \frac{\partial \mathbf{u}}{\partial t} + \mathbf{u} \cdot \nabla \mathbf{u} &= -g\nabla \eta + \nabla \cdot (\nu \nabla \mathbf{u}) + \mathbf{f} \text{ in } \Omega, \end{aligned} \tag{1}$$

where $\eta(\mathbf{x}, t)$ is the elevation (unit : m) of the free surface, $H(\mathbf{x}, t)$ the total depth (unit : m) of the water column $H = \eta + b$, $b(\mathbf{x})$ the bathymetry (unit : m), (see Figure 1 for visual representation of these quantities), $\mathbf{u} = (u, v)$ the velocity field (unit : m/s), g the constant of gravitational acceleration (unit : m/s^2), ν the kinematic viscosity, $\mathbf{f} = (f_x, f_y)$ the source, and Ω the computational domain.

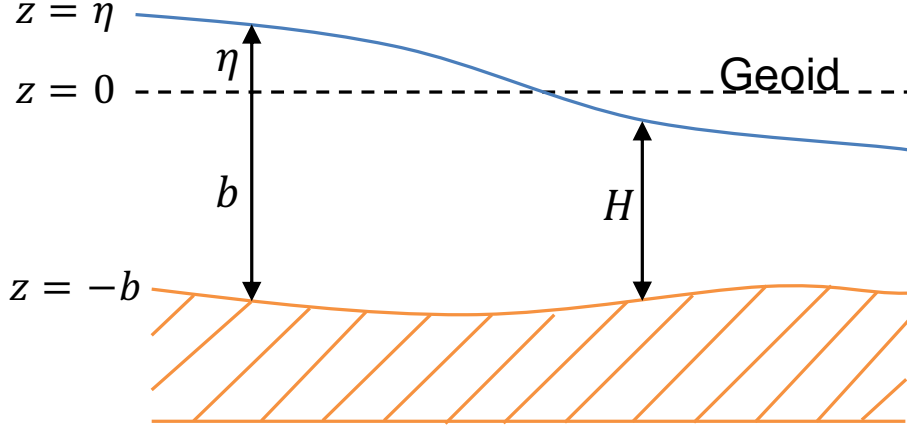


Figure 1: A illustration of the Geoid and standard shallow water quantities.

We assume the driving forces of the water column motion to be atmospheric pressure, wind, and bottom friction. Hence, the source \mathbf{f} takes the form:

$$\mathbf{f} = -g\nabla \left(\frac{p_{atm}}{g\rho_w} \right) + \frac{C_d \rho_a}{H \rho_w} \|\mathbf{w}\| \mathbf{w} - \frac{C_b}{H} \|\mathbf{u}\| \mathbf{u}, \quad (2)$$

where C_d is the wind drag coefficient, C_b the bottom friction coefficient, ρ_a the density of air, ρ_w the density of water, $\mathbf{w} = (w_x, w_y)$ the wind speed (typically at a height of 10 meters above the surface), the atmospheric pressure p_{atm} , and $\|\cdot\|$ denotes the vector magnitude. To ensure solvability of the SWE in the SSWM, we also need proper initial and boundary condition. We consider homogeneous initial conditions for both velocity and elevation in all cases unless explicitly noted. We also consider the following types of boundary conditions: free-slip, specified elevation, and no-normal flow. To identify these conditions, we separate the boundary Γ of the domain Ω into two disjoint parts: $\Gamma = \Gamma_{cl} \cup \Gamma_{op}$. A free-slip boundary condition is applied to the entire boundary:

$$\nabla \mathbf{u} \cdot \mathbf{n} = \mathbf{0} \text{ on } \Gamma. \quad (3)$$

The no-normal flow (also referred to as impenetration) boundary condition is applied to the closed, or land, portion of the boundary:

$$\mathbf{u} \cdot \mathbf{n} = \mathbf{0} \text{ on } \Gamma_{cl}. \quad (4)$$

Finally, an elevation boundary condition is applied to the open, or ocean, part of the boundary:

$$\eta = r \text{ on } \Gamma_{op} \quad (5)$$

2.2. Sources of Uncertainty

In shallow water systems, uncertainty can be induced from several sources, e.g., initial conditions, boundary conditions, bathymetry, bottom friction coefficients, and wind drag coefficients. This leads to uncertainty in the surface elevation and velocity field in the SWE (1). For the general setting of the stochastic Galerkin (SG) method, we introduce polynomial chaos representations of the uncertainties. In particular, we use the generalized polynomial chaos (gPC) expansion, see e.g., [17]. If we consider the wind drag coefficient $C_d(\mathbf{x}, t; \xi)$ and bottom drag coefficient $C_b(\mathbf{x}, t; \xi)$, these are represented by the following expansions:

$$\begin{aligned} C_d(\mathbf{x}, t; \xi) &= \sum_{i=0}^M C_i^d(\mathbf{x}, t) \Phi_i(\xi(\omega)), \\ C_b(\mathbf{x}, t; \xi) &= \sum_{j=0}^M C_j^b(\mathbf{x}, t) \Phi_j(\xi(\omega)), \end{aligned} \quad (6)$$

where $\xi(\theta)$ is a vector of random variables, the C_i 's the expansion coefficients of the i 'th modes, and Φ_i , $i = 0, 1, \dots, M$ the orthonormal gPC bases. The relationship between $\xi(\theta)$ and Φ_i is established by the Wiener-Askey scheme from [17]. Using gPC expansions, we also represent the remaining uncertain sources analogous to (6). The orthogonality property of the gPCs allows us to compute the mode coefficients by taking the inner product with $\Phi_k(\xi(\theta))$, e.g.,

$$C_i^d(\mathbf{x}, t) = \int_{\Theta} C_d(\mathbf{x}, t; \xi) \Phi_k(\xi(\theta)) d\theta \text{ for } k = 0, \dots, M. \quad (7)$$

2.3. Stochastic Formulation

To derive the stochastic formulation of our SSWM, we use the same set of random variables as for the uncertainties in Section 2.2 to represent the uncertain outputs η and \mathbf{u} :

$$\begin{aligned} \mathbf{u}(\mathbf{x}, t; \xi) &= \sum_{i=0}^M \mathbf{u}_i(\mathbf{x}, t) \Phi_i(\xi(\theta)), \\ \eta(\mathbf{x}, t; \xi) &= \sum_{j=0}^M \eta_j(\mathbf{x}, t) \Phi_j(\xi(\theta)). \end{aligned} \quad (8)$$

This choice allows us to again exploit the orthogonality property of gPC expansions. Hence, we substitute the expansions (8) into the SWE (1), integrate over the probability space $L_2(\Theta, \Sigma, P)$ (Θ the event space, Σ the σ -field on Θ , and P the probability measure), and apply the orthogonality property to obtain the discrete stochastic formulation for each stochastic mode k :

$$\frac{\partial \eta_k}{\partial t} + \nabla \cdot (H_i \mathbf{u}_j) \langle ijk \rangle = 0 \quad \text{on } \Omega, \quad (9a)$$

$$\frac{\partial \mathbf{u}_k}{\partial t} + \mathbf{u}_i \cdot \nabla \mathbf{u}_j \langle ijk \rangle = -g \nabla \eta_k + \nabla \cdot (\nu \nabla \mathbf{u}_k) + \mathbf{f}_k \quad \text{on } \Omega, \quad (9b)$$

$$u_k(\mathbf{x}, 0) = u_k^0(\mathbf{x}) \quad \text{at time } t = 0, \quad (9c)$$

$$\eta_k(\mathbf{x}, 0) = \eta_k^0(\mathbf{x}) \quad \text{at time } t = 0. \quad (9d)$$

In (9), $\langle ijk \rangle = \int_{\theta \in \Theta} \Phi_i(\xi(\theta)) \Phi_j(\xi(\theta)) \Phi_k(\xi(\theta)) d\theta$, and \mathbf{f}_k is:

$$\mathbf{f}_k = -g \nabla \left(\frac{p_{atm.}}{g \rho_w} \right) \delta_{0k} + \frac{C_k^d \rho_a}{H_0 \rho_w} \|\mathbf{w}\| \mathbf{w} - \frac{C_i^b}{H_0} \|\mathbf{u}_0\| \mathbf{u}_j \langle ijk \rangle, \quad (10)$$

where C_i^d is the i^{th} mode of the wind drag coefficient $C_d(\mathbf{x}, t; \xi)$, and C_j^b is the j^{th} mode of the bottom drag coefficient $C_b(\mathbf{x}, t; \xi)$ obtained by gPC expansions. Note that in the definition of \mathbf{f}_k (10), we use the mean of the total depth H_0 instead of the n^{th} -mode of total depth H_n to avoid its high order summation terms in the denominators. Second, we have also linearized the stochastic nonlinear bottom shear stress and wind stress terms. By integrating over probability space, the stochastic problem becomes deterministic: *Given the initial conditions in (9c) and (9d), C_k^d , and C_k^b , find the stochastic modes of $\mathbf{u}_k(\mathbf{x}, t)$ and $\eta_k(\mathbf{x}, t)$, $k = 0, 1, \dots, M$, such that the conservation law (9a) and (9b) is satisfied.*

2.4. Spatial Discretization

Let \mathbf{V} denote the vector-valued trial and test function space and Q the scalar-valued trial and test function space. The regularity requirements of the equivalent weak form of the SWE (1) lead us to the definitions:

$$\begin{aligned} \mathbf{V} &= \{\mathbf{u} \in \mathbf{H}^1(\Omega) \times (0, T) : \mathbf{u} \cdot \mathbf{n} = 0 \text{ on } \Gamma_{cl}\}, \\ Q &= \{\eta \in H^1(\Omega) \times (0, T) : \eta = r \text{ on } \Gamma_{op}\}. \end{aligned} \quad (11)$$

Also denote by $\mathbf{v}_k \in \mathbf{V}$ the test function for velocity modes in the momentum equation (9b) and $q_k \in Q_0$ as the test function for the elevation modes in the continuity equation (9a). Q_0 is the restriction of Q to functions that vanish on the global boundary:

$$Q_0 = \{q \in H^1(\Omega) : q = 0 \text{ on } \Gamma\}. \quad (12)$$

Multiplication of (9a) and (9b) with the test functions (\mathbf{v}_k, q_k) and subsequent integration by parts of the divergence and viscous terms leads to the weak formulation:

Find $(\mathbf{u}_k, \eta_k) \in \mathbf{V} \times Q$, such that $\forall (\mathbf{v}_k, q_k) \in \mathbf{V} \times Q_0, \quad t \in (0, T) :$

$$\begin{aligned} \left(\frac{\partial \eta_k}{\partial t}, q_k\right)_\Omega - (H_i \mathbf{u}_j \langle ijk \rangle, \nabla q_k)_\Omega &= 0, \\ \left(\frac{\partial \mathbf{u}_k}{\partial t}, \mathbf{v}_k\right)_\Omega + (\mathbf{u}_i \cdot \nabla \mathbf{u}_j \langle ijk \rangle, \mathbf{v}_k)_\Omega &= -(g \nabla \eta_k, \mathbf{v}_k)_\Omega - (\nu \nabla \mathbf{u}_k, \nabla \mathbf{v}_k)_\Omega + (\mathbf{f}_k, \mathbf{v}_k)_\Omega, \end{aligned} \quad (13)$$

where we use inner product notation, i.e., $(\cdot, \cdot)_\Omega$ denotes the L_2 inner product over Ω . The boundary terms from integration by parts vanish due to application of boundary conditions in (13).

The stochastic weak formulation (13) can be directly discretized in space for each mode k by applying the Bubnov-Galerkin method. Hence, we select discrete subspaces $\mathbf{V}^h \times Q^h \subset \mathbf{V} \times Q$, which consists of Lagrange polynomials of order two and one for \mathbf{V}^h and Q^h , respectively. This type of discretization is often referred to as a Taylor-Hood finite element method and the discretized weak form is shown in (14). In practice, we shall always augment the discretized weak formulation with stabilization techniques to ensure stable discretizations of the stochastic weak formulation.

Find $(\mathbf{u}_k^h, \eta_k^h) \in \mathbf{V}^h \times Q^h$, such that $\forall (\mathbf{v}_k^h, q_k^h) \in \mathbf{V}^h \times Q_0^h, \quad t \in (0, T) :$

$$\begin{aligned} \left(\frac{\partial \eta_k^h}{\partial t}, q_k^h\right)_\Omega - (H_i^h \mathbf{u}_j^h \langle ijk \rangle, \nabla q_k^h)_\Omega &= 0, \\ \left(\frac{\partial \mathbf{u}_k^h}{\partial t}, \mathbf{v}_k^h\right)_\Omega + (\mathbf{u}_i^h \cdot \nabla \mathbf{u}_j^h \langle ijk \rangle, \mathbf{v}_k^h)_\Omega &= -(g \nabla \eta_k^h, \mathbf{v}_k^h)_\Omega - (\nu \nabla \mathbf{u}_k^h, \nabla \mathbf{v}_k^h)_\Omega + (\mathbf{f}_k, \mathbf{v}_k^h)_\Omega, \end{aligned} \quad (14)$$

2.5. Time Discretization

As the computational cost of our stochastic system scales linearly with the number of modes used to represent those uncertainties, we employ the Incremental Pressure Correction

Scheme (IPCS) [20, 21]. This operator splitting scheme decouples the hyperbolic system and enables us to solve surface elevation and velocity independently thereby reducing the computational cost. We omit the details of the IPCS here for the sake of brevity and include only an overview in Algorithm 1 and refer the interested reader to [22] for details. Note that the IPCS algorithm is compatible with any implicit time stepping method, in this work we exclusively employ the backward Euler method whereas in [22] others are considered.

Algorithm 1: IPCS time discretization scheme

Given \mathbf{u}^0 and η^0 ;

while $t \leq T$ **do**

1. Given the surface elevation η^n , solve for the IPCS "tentative velocity" $\tilde{\mathbf{u}}^{n+1}$,
see [22];
2. Given the tentative velocity $\tilde{\mathbf{u}}^{n+1}$, compute the surface elevation η^{n+1} ;
3. Given the surface elevation η^{n+1} , compute the velocity \mathbf{u}^{n+1} ;

end

Result: A time series of \mathbf{u} and η ;

2.6. Cross-mode stabilization methods

It is well known that standard Bubnov-Galerkin FE method leads to unstable numerical schemes for convection-dominated flows which exhibits itself as oscillations in the FE solution. Furthermore, the stochastic weak formulation (13) leads to a deterministic modes-coupled hyperbolic system (see $\mathbf{u}_i \cdot \nabla \mathbf{u}_j \langle ijk \rangle$ term in (13)), in which the resulting linear system of equations that is M times larger than the corresponding deterministic SWE. The effect of this coupling is stronger instabilities in the FE approximation. To seek a stable discrete solution of each mode \mathbf{u}_k^h and η_k^h , we propose three cross-mode stabilization methods which can be applied independently or simultaneously to the discretized stochastic weak formulation. We also refer interested readers to [22] for details on this novel multiple stabilization for the fully deterministic system. The starting point for the stabilized methods is the discretized weak formulation (14). For notational convenience, we drop the superscript h in this section as it is understood that the stabilization methods are only applied to the discrete case.

2.6.1. Cross-mode Streamlined Upwind Petrov Galerkin Method

The classical streamlined upwind Petrov-Galerkin (SUPG) method for the Navier-Stokes equations was introduced by Brooks and Hughes in [23]. The SUPG stabilizes the spatial FE discretization by adding artificial diffusion over element interiors along the streamline direction. Based on the standard SUPG method, we propose to add the following terms to (14):

$$\sum_{e \in N_e} \tau_{SUPG} (\mathbf{R}_k(\tilde{\mathbf{u}}_k^{n+1}), \mathbf{u}_k^* \cdot \nabla \mathbf{v}_k)_{\Omega_e}, \quad k = 0, 1, \dots, M, \quad (15)$$

where $\mathbf{u}_k^* = \frac{3}{2}\mathbf{u}_k^n - \frac{1}{2}\mathbf{u}_k^{n-1}$, and $\tilde{\mathbf{u}}_k^{n+1}$ is the IPCS tentative velocity of the k -th mode at $(n+1)$ th time step (see details of both quantities in the introduction of the IPCS scheme in [22]). M is the total number of gPC functions, N_e the number of elements in the FE mesh, τ_{SUPG} the stabilization parameter, and $\mathbf{R}_k(\tilde{\mathbf{u}}_k^{n+1})$ is the residual form of the original stochastic SWE:

$$\mathbf{R}_k(\tilde{\mathbf{u}}_k^{n+1}) = \frac{1}{\Delta t} (\tilde{\mathbf{u}}_k^{n+1} - \mathbf{u}_k^n) + \mathbf{u}_i^* \cdot \nabla \tilde{\mathbf{u}}_j^{n+1} \langle ijk \rangle + g \nabla \eta_k^n - \nabla \cdot \nu \nabla \tilde{\mathbf{u}}_k^{n+1} - \mathbf{f}_k^{n+1}. \quad (16)$$

The number of gPC functions M depends on the gPC order N and the dimension d of the probability space as the binomial coefficient:

$$M = \binom{N+d}{N}.$$

Based on the works of Tezduyar [24, 25], we select τ_{SUPG} :

$$\tau_{SUPG} = \left(\frac{2}{\Delta t} + \frac{2\|\mathbf{u}_0^n\|}{h_e} + \frac{4\nu}{h_e^2} \right)^{-1}, \quad (17)$$

where h_e is the radius of the circumscribed circle of each element and \mathbf{u}_0^n is the mean mode of \mathbf{u} at n^{th} time step. Note that the cross-mode SUPG preserves the consistency of the classical SUPG as $\mathbf{R}_k(\tilde{\mathbf{u}}_k^{n+1})$ vanishes if $\tilde{\mathbf{u}}_k^{n+1}$ is the solution of the stochastic PDE (9).

2.6.2. Cross-mode Discontinuity Capturing Method

In the numerical stabilization of the deterministic SWE using FE methods, it is often not sufficient to apply only the SUPG method to stabilize the discrete systems. Since SUPG adds diffusive effects only along the streamlines, other techniques may also be needed. This problem is further exaggerated in our SSWM due to the coupled modes. Hence, we also

incorporate another residual based stabilization method, the discontinuity capturing (DC) method of Hughes *et al.* [26]. We therefore add the following to (14):

$$\sum_{e \in N_e} \tau_{DC}^1 \left(\mathbf{u}_{k||u_1}^* \cdot \nabla v_{k1}, R_{k1}(\tilde{\mathbf{u}}_k^{n+1}) \right)_{\Omega_e} + \sum_{e \in N_e} \tau_{DC}^2 \left(\mathbf{u}_{k||u_2}^* \cdot \nabla v_{k2}, R_{k2}(\tilde{\mathbf{u}}_k^{n+1}) \right)_{\Omega_e}, \quad (18)$$

where $\mathbf{v}_k = (v_{k1}, v_{k2})$ is the test function for the k -th mode, R_{k1}, R_{k2} are the x, y components of the residual form $\mathbf{R}_k(\tilde{\mathbf{u}}_k^{n+1})$, see (16), $\mathbf{u}_{k||u_1}^*$ the projection of \mathbf{u}_k^* onto $\nabla \tilde{u}_{k1}^{n+1}$, $\tilde{\mathbf{u}}_{k||u_2}^*$ the projection of \mathbf{u}_k^* onto $\nabla \tilde{u}_{k2}^{n+1}$, and $\tilde{\mathbf{u}}_k^{n+1} = (\tilde{u}_{k1}^{n+1}, \tilde{u}_{k2}^{n+1})$. The projection operators are illustrated in Figure 2 and are defined by:

$$\mathbf{u}_{k||u_1}^* = \frac{\mathbf{u}_k^* \cdot \nabla \tilde{u}_{k1}^{n+1}}{|\nabla \tilde{u}_{k1}^{n+1}|^2} \nabla \tilde{u}_{k1}^{n+1}, \quad (19)$$

$$\mathbf{u}_{k||u_2}^* = \frac{\mathbf{u}_k^* \cdot \nabla \tilde{u}_{k2}^{n+1}}{|\nabla \tilde{u}_{k2}^{n+1}|^2} \nabla \tilde{u}_{k2}^{n+1}. \quad (20)$$

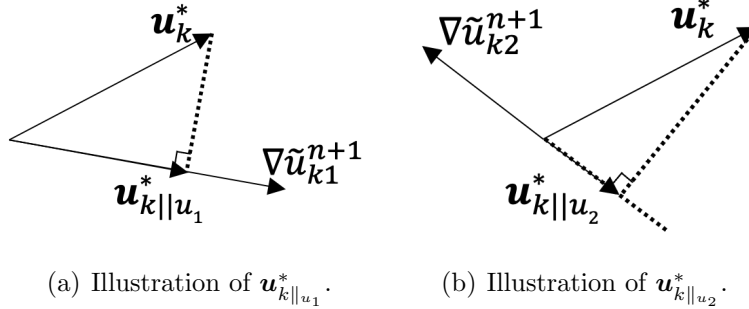


Figure 2: Projections of velocity gradient modes.

τ_{DC}^1, τ_{DC}^2 are the DC stabilization parameters:

$$\tau_{DC}^1 = \left(\frac{2}{\Delta t} + \frac{2\|\mathbf{u}_{k||u}^*\|}{h_e} + \frac{4\nu}{h_e^2} \right)^{-1}, \quad \tau_{DC}^2 = \left(\frac{2}{\Delta t} + \frac{2\|\mathbf{u}_{k||v}^*\|}{h_e} + \frac{4\nu}{h_e^2} \right)^{-1}. \quad (21)$$

To avoid an overly stabilized effect and therefore nonphysical solutions from both SUPG and DC, we adjust the parameters in (21) as follows:

$$\begin{aligned} \tilde{\tau}_{DC}^1 &= \max(0, \tau_{DC}^1 - \tau_{SUPG}), \\ \tilde{\tau}_{DC}^2 &= \max(0, \tau_{DC}^2 - \tau_{SUPG}). \end{aligned} \quad (22)$$

The cross-mode DC method is also consistent, as the residual term goes to zero for the true solution of each stochastic mode.

2.6.3. Cross-mode Continuous Interior Penalty Method

The last stabilization method we employ in our coupled system follows the continuous interior penalty (CIP) method [27]. Thus, we penalize inter-element discontinuities in the test functions by adding the following term to our discretized weak formulation (14):

$$\sum_{e \in N_e} \sigma_{CIP} \cdot \bar{h}_e^{-2} \cdot \text{avg}(|\tilde{\mathbf{u}}_k^{n+1} \cdot \mathbf{n}|) \left(\llbracket \nabla \mathbf{v}_k \cdot \mathbf{n} \rrbracket, \llbracket \nabla \tilde{\mathbf{u}}_k^{n+1} \cdot \mathbf{n} \rrbracket \right)_{\partial \Omega_e}, \quad (23)$$

where σ_{CIP} is a positive constant, $\llbracket \cdot \rrbracket$ the jump operator for adjacent elements, $\text{avg}(\cdot)$ represents the average operator over adjacent elements, and \bar{h}_e is the maximum edge length in an element Ω_e . Note that the cross-mode CIP method is also consistent as the added jump terms vanish for sufficiently smooth stochastic solutions.

3. Verification of the SSWM

To perform a verification process of the proposed SSWM framework, we will perform three idealized numerical tests that represent small scale short term shallow water flows and two realistic numerical tests that represents large scale long term applications. The corresponding numerical program is a python program solving the nonlinear SSWM for shallow water flows. It is built on the finite element package FEniCS [28, 29, 30, 31, 32, 33] and the statistics package Chaospy [34]. Chaospy is used for P-integration of the gPC over probability space in the SSWM discretization from FEniCS. The program is designed in four modules and its structure is visually presented in Figure 3.

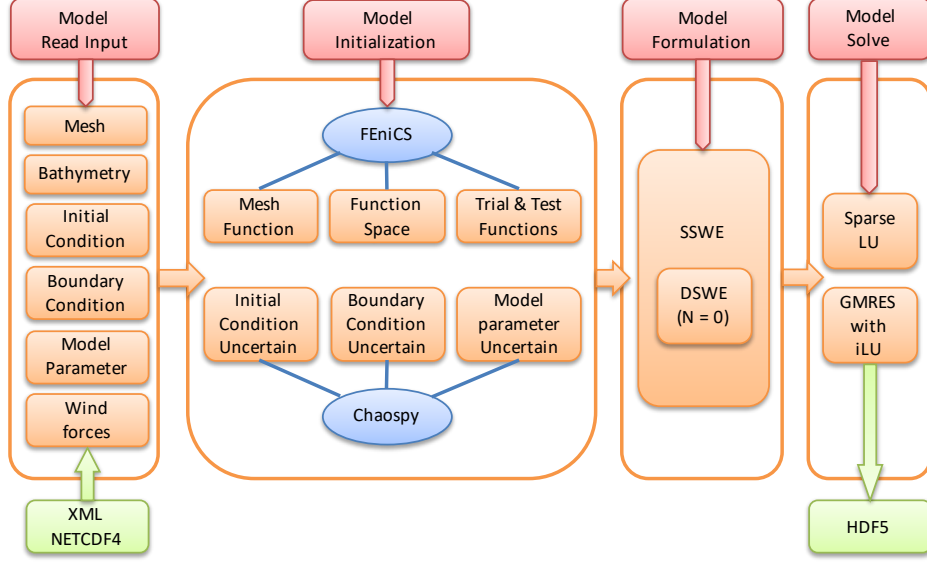


Figure 3: A illustration of the SSWM code structure.

To validate the numerical implementations of SSWM and demonstrate the effectiveness of the proposed cross-mode stabilization methods, we will conduct a two-step process. First, we verify the deterministic shallow water model (DSWM), which is a degraded (i.e., polynomial chaos order $N = 0$) SSWM. This verification is done with respect to analytical solutions and well-established model simulation results. Second, we validate the SSWM surrogates pointwise by comparison to its Monte-Carlo counterparts. Note that in the second validation step, the surrogate functions $f(\mathbf{x}, t; \boldsymbol{\xi})$, we first fix the time t , and compare the SSWM surrogate over all sample grids $\boldsymbol{\xi}$, we subsequently fix the sample grids $\boldsymbol{\xi}$ and compare the SSWM surrogate over all time steps. This multi-dimensional validation ensures a comprehensive pointwise comparison between the model surrogate and its counterparts.

For verification of the SSWM, in the three small scale idealized test cases we consider an uncertain initial condition (case 1), uncertain bathymetry (case 2), and uncertain boundary conditions (case 3). For the large scale cases we consider an uncertain wind drag coefficient (both case 4 and case 5). We will use the two-step verification and validation framework in these tests to comprehensively validate the SSWM.

3.1. Numerical Tests

In this section, we define and describe the set up of the test cases we consider in this verification and validation process.

3.1.1. Slosh Test Case With Uncertain Initial Condition

As an initial test case, we consider a rectangular domain with length $L = 100m$, width $W = 50m$, and constant water depth $H = 20m$. The four boundaries are closed, with a free slip boundary condition. The surface elevation is initially a west to east varying cosine shaped perturbation, with an amplitude of $0.1m$ and a wavelength of $200m$. The water velocity is initially zero everywhere, we assume inviscid flow, i.e., $\nu = 0$. No external forcing is applied, and the time step in the IPCS is set to 0.5 seconds. The total simulation time is 50 seconds and we use the uniform triangular mesh shown in Figure 4. In this test case, the

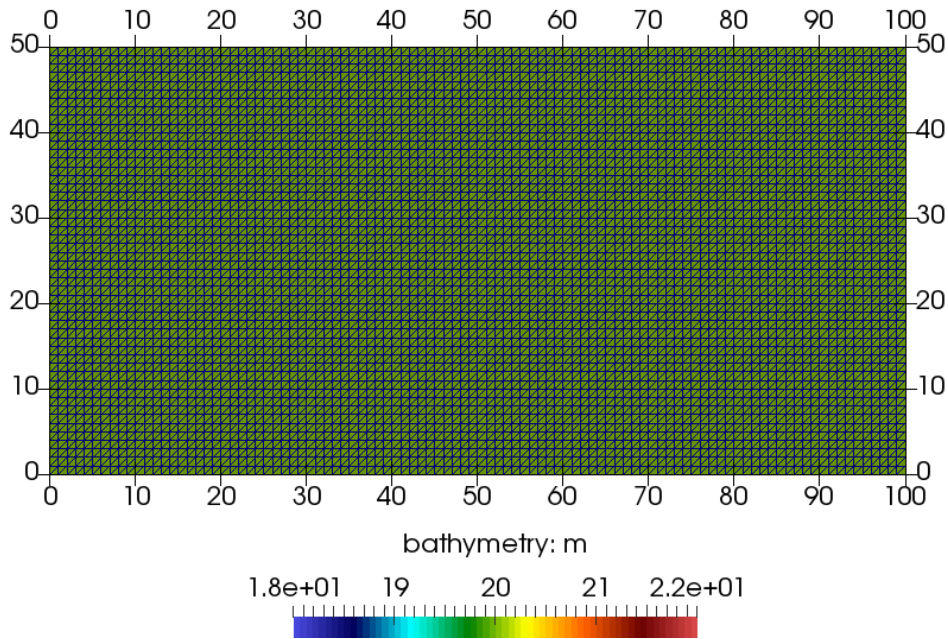


Figure 4: Slosh test case: Mesh and bathymetry

uncertainty of the initial condition is assumed to take the form $\eta = 0.1\xi_1\xi_2 \cos(\pi x/100.0)$, where ξ_1, ξ_2 are both uniformly distributed $\xi_1 \sim U(0.8, 1.2)$, $\xi_2 \sim U(1.0, 2.0)$, i.e., two-dimensional generalized polynomial chaos, and the stochastic order $N = 3$. In this test case, no cross-mode stabilization is added to the computations as the mesh and time step are both sufficiently fine to ensure stable computations.

3.1.2. Hump Test Case With Uncertain Bathymetry

In the second test case, we again consider a rectangular domain, in this case it is $1000m$ long and $200m$ wide. The bathymetry in this case consists of a hump, see Figure 5, and is

given by:

$$b = \begin{cases} -3.0 \left(\frac{x - 500.0}{100.0} \right)^4 + 6.0 \left(\frac{x - 500.0}{100.0} \right)^2 + 2.0, & 400m < x < 600m \\ 5.0, & \text{else} \end{cases} \quad (24)$$

The domain is closed with free slip boundary conditions on the north, south, and west sides, whereas the east side is a tidal boundary where the sinusoidal function $0.1 \sin(\pi t/20)$ is prescribed. The initial water elevation and velocities are all zero. There is no viscosity in the domain, no external forcing is applied, and the time step in the IPCS is set to 1.0 seconds. The total simulation time is 300 seconds and we use the uniform mesh shown in Figure 5. We further assume the uncertainty of bathymetry to be of the form:

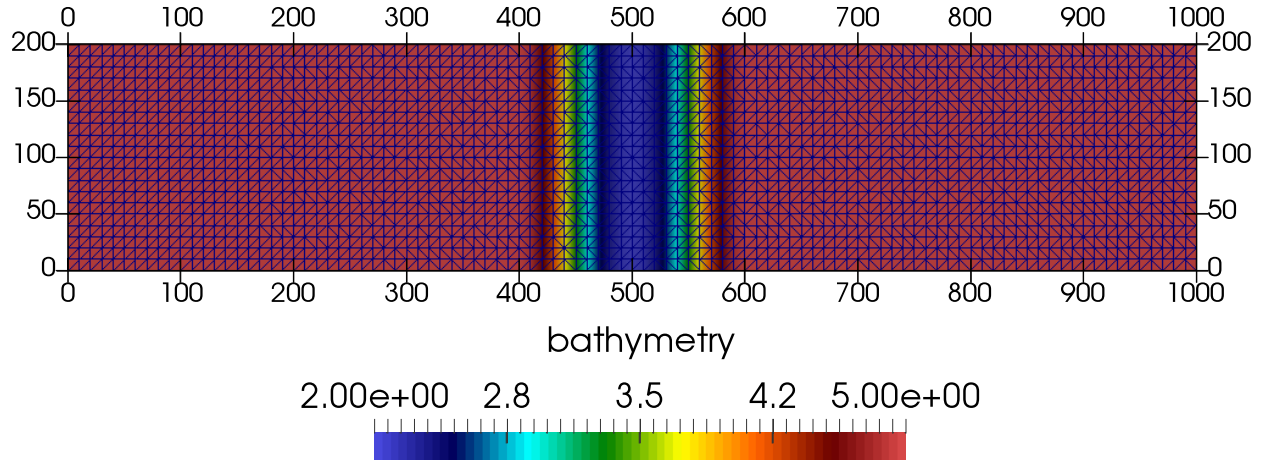


Figure 5: Hump test case: Mesh and bathymetry

$$b = \begin{cases} -3.0\xi_1 \left(\frac{x - 500.0}{100.0} \right)^4 + 6.0\xi_2 \left(\frac{x - 500.0}{100.0} \right)^2 + 2.0, & 400m < x < 600m \\ -3.0\xi_1 + 6.0\xi_2 + 2.0, & \text{else} \end{cases} \quad (25)$$

where ξ_1, ξ_2 are assumed to be uniformly distributed, $\xi_1 \sim U(0.8, 1.2)$ and $\xi_2 \sim U(0.9, 1.1)$. We again utilize two-dimensional gPC and set the stochastic order $N = 3$. As in the preceding case, the computations are numerically stable due to the selected mesh resolution and time step.

3.1.3. Idealized Inlet Test Case With Uncertain Boundary Condition

To demonstrate the capability of our methodology to handle complicated scenarios, we consider an idealized inlet test case. The domain consists of a rectangular harbor connected to the open ocean via a narrow channel. All boundaries are closed except the western, which is open. The bathymetry varies linearly from 19m at the open ocean boundary to 5m at the entrance of the channel. Furthermore, there is a hump near the entrance of the channel, approximately 750m in diameter with a maximum height of 2m. This hump is used to simulate the physics of an ebb shoal. These commonly appear in coastal channels and are formed due to decelerated flows depositing transported sediments near channel exits. The mesh and bathymetry are shown in Figure 6. To the western boundary we apply M2

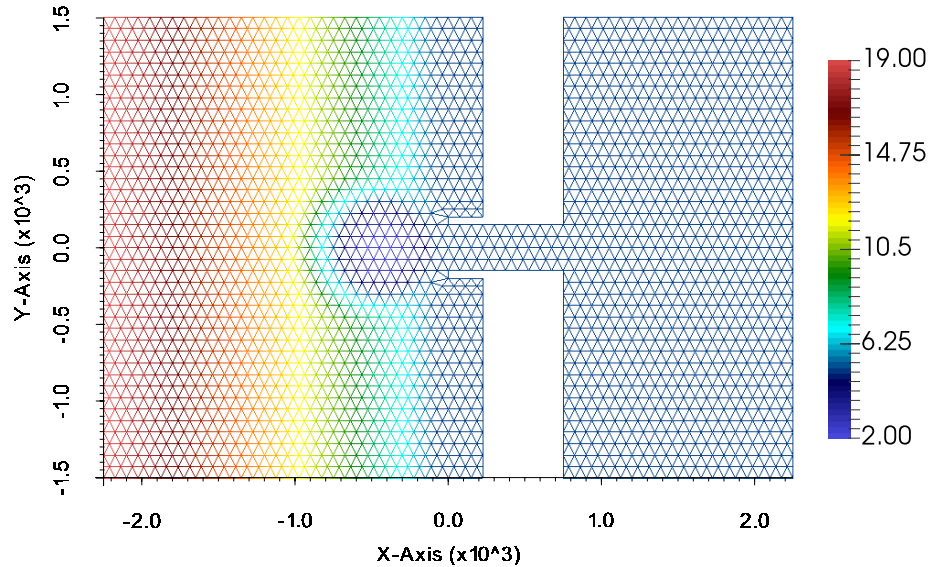


Figure 6: Idealized inlet test case mesh and bathymetry.

tides[35], and the remaining boundaries are closed with free slip conditions. The M2 tides follow $\eta = A \sin(\Omega t)$, where A is an amplitude of 0.75m, Ω is an angular frequency of 1.41×10^{-4} rad/s. We apply homogeneous initial conditions, set the kinematic viscosity to 10^{-6} , and the bottom friction coefficient is set to $C_b = 0.003$. The time step in the IPCS is set to 447 seconds and the simulation covers five M2 tidal cycles, approximately 2.5 days. To stabilize the FE discretizations in this test case, we apply all three cross-mode stabilization techniques from Section 2.6 with τ_{SUPG} and τ_{DC} , see (17) and (22) and the CIP stabilization

parameter σ_{CIP} set to 0.75. In this test case, we assume the uncertainty of the boundary condition to be of the form $\eta = 0.2\xi_1 \sin(\Omega t)$, where ξ_1 is uniformly distributed, given as $\xi_1 \sim U(1.0, 2.0)$, i.e., one-dimensional gPC is utilized and we set the stochastic order $N = 3$.

3.1.4. Historical Hurricane Test Cases for the Gulf of Mexico and Historical Hurricanes With Uncertain Wind Drag Coefficient

In these two tests, we choose the Gulf of Mexico as the domain of interest and the historical hurricanes Harvey (2017) and Ike (2008), see Figures 7 and 8 for the mesh, physical domain and maximum hurricane winds. These hurricanes are selected as they are representative of two types of hurricanes in the Gulf of Mexico, a large slow moving hurricane (Ike) and a smaller fast moving hurricane (Harvey). A closed free-slip boundary condition is applied on the entire domain and the sea water is initially at rest. The kinematic viscosity is set to 10^{-6} and the bottom friction coefficient is fixed: $C_b = 0.003$. In these cases, seawater motion is externally forced by the hurricane winds only. The wind fields are obtained from the National Hurricane Center's best track HURDAT2 database and we apply a Powell scheme [36] to determine the wind drag coefficient. The time step in the IPCS is set to 447 seconds and the simulations cover selected time spans for both hurricanes. Hence, for Hurricane Ike 2.5 days starting September 11 2008 12:00pm and for Hurricane Harvey 6 days starting at August 24 2017 6:00pm Central Daylight Time. To stabilize the FE discretizations in these test cases, we apply all three cross-mode stabilization techniques from Section 2.6 with τ_{SUPG} and τ_{DC} , see (17) and (22) and the CIP stabilization parameter σ_{CIP} set to 9.0.

In these large scale test cases, we assume that the wind drag coefficient is uncertain because this parameter is well known to significantly impact the maximum surge during hurricane events, see e.g., [37]. In the Powell scheme we use to ascertain the wind drag parameter C_d^{Powell} , the range of this coefficient is limited to $[0.0001, 0.0005]$ and it varies linearly with the magnitude of wind velocity in each quadrant relative to the hurricane center. Hence, we assume the uncertain wind drag coefficient takes the same form of $C_d = \xi_1 C_d^{Powell}$, where ξ_1 is assumed to be uniformly distributed; i.e., $\xi_1 \sim U(0.8, 1.2)$, i.e., one-dimensional gPC is utilized here and we set the stochastic order $N = 1$.

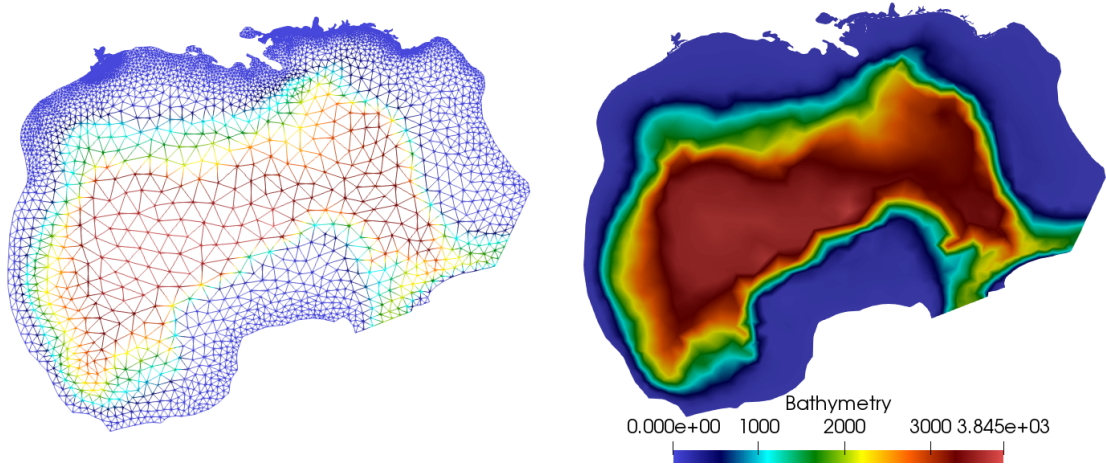


Figure 7: Mesh and Bathymetry for the hurricane test cases.

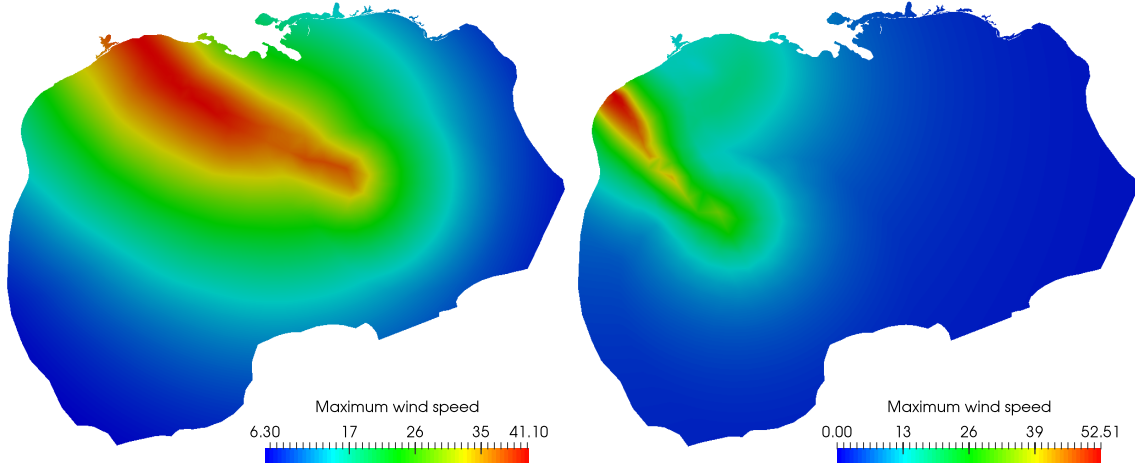


Figure 8: Maximum wind speed during Hurricanes Ike (left) and Harvey (right).

3.2. Verification of the Deterministic Part of the Stochastic Model

To verify the deterministic part of the stochastic model, we first check the rate of convergence of the deterministic model for the slosh test case of Section 3.1.1. Furthermore, for comparison against two existing hydraulic models, ADCIRC [38, 39] and ADH [40], we consider the hump test case of Section 3.1.2 and Inlet test case of Section 3.1.3, respectively. Finally, we consider Hurricane Ike in the Gulf of Mexico and compare the deterministic SSWM solution against the ADCIRC model.

3.2.1. Convergence of the Deterministic SSWM

To assess the convergence properties of our deterministic model, we consider an analytical solution to the slosh test case from [41]:

$$\begin{aligned}\eta(x, y, t) &= a \cos\left(\frac{\pi}{L}x\right) \cos\left(\frac{\pi\sqrt{gD}}{L}t\right), \\ u(x, y, t) &= \frac{a\sqrt{gD}}{D} \sin\left(\frac{\pi}{L}x\right) \sin\left(\frac{\pi\sqrt{gD}}{L}t\right), \\ v(x, y, t) &= 0,\end{aligned}\tag{26}$$

where D denotes bathymetry. We consider convergence of the FE error in the standard L_2 norm:

$$\|e\|_{\Omega} = \sqrt{\int_{\Omega} (\phi - \phi_h)^2 d\Omega},\tag{27}$$

where ϕ is the analytic solution, and ϕ_h is the FE solution. We compute the FE solution with increasing mesh resolution of size $h = \{10m, 5m, 2.5m, 1.25m, 0.625m\}$, we obtain the rate of convergence for both surface elevation and water velocity and present the results in Table 1. As shown in this table, the error surface elevation reaches its optimal L^2 convergence rate

Mesh	h	<i>Surface elevation</i>		<i>Water velocity</i>	
		$\ e\ _{L^2}$	$p = 1$	$\ e\ _{L^2}$	$p = 2$
h1	10	4.0929×10^{-2}	-	3.8166×10^{-4}	-
h2	5	1.0268×10^{-2}	1.9949	1.2576×10^{-4}	1.6016
h3	2.5	2.5694×10^{-3}	1.9987	4.2418×10^{-5}	1.5680
h4	1.25	6.4249×10^{-4}	1.9997	1.4591×10^{-5}	1.5396
h5	0.625	1.6063×10^{-4}	1.9999	5.0834×10^{-6}	1.5212

Table 1: Slosh test case: L_2 convergence rate

of order 2. However, the rate of convergence for the velocity is sub optimal. The reason for this is found in the IPCS scheme (see Section 3.2.3 in [22]), which neglects certain high order terms.

3.2.2. Comparison With the ADCIRC Model

The convergence properties considered in the previous section as well as further studies presented in [22] give us confidence in the approximation properties of our deterministic

SSWM. We now further verify our model by comparison against results from the ADCIRC model for the hump test case described in Section 3.1.2. To this end, we consider a comparison of the time series of the elevation and the x component of the velocity field at the points $(250.0m, 100.0m)$ and $(750.0m, 100.0m)$. The comparison is presented in Figures 9 and 10, where the agreement between the two models is very good for both solution variables throughout the simulation.

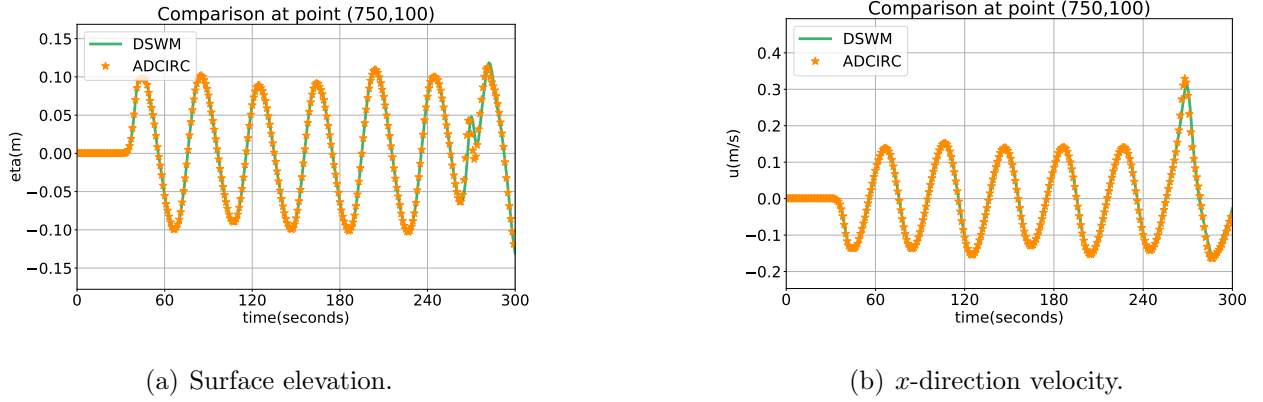


Figure 9: Comparison between the new model and ADCIRC.

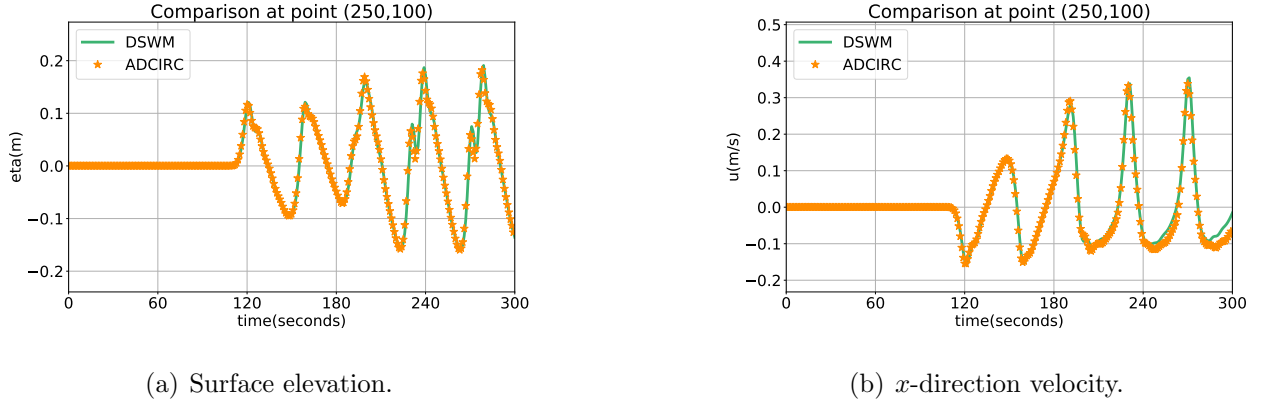


Figure 10: Comparison between the new model and ADCIRC.

3.2.3. Comparison With the ADH Model

As another verification of the deterministic model, we consider the inlet test case and compare our results to the ADH model. This test is challenging due to the shocks that form at the exit of the narrow channel. In Figures 11 and 12, we present a visual comparison between

the two models for the velocity field at two selected times. In Figure 13, the corresponding absolute errors in velocity magnitude are shown. Overall, the two models agree on the flow characteristics with certain localized discrepancies.

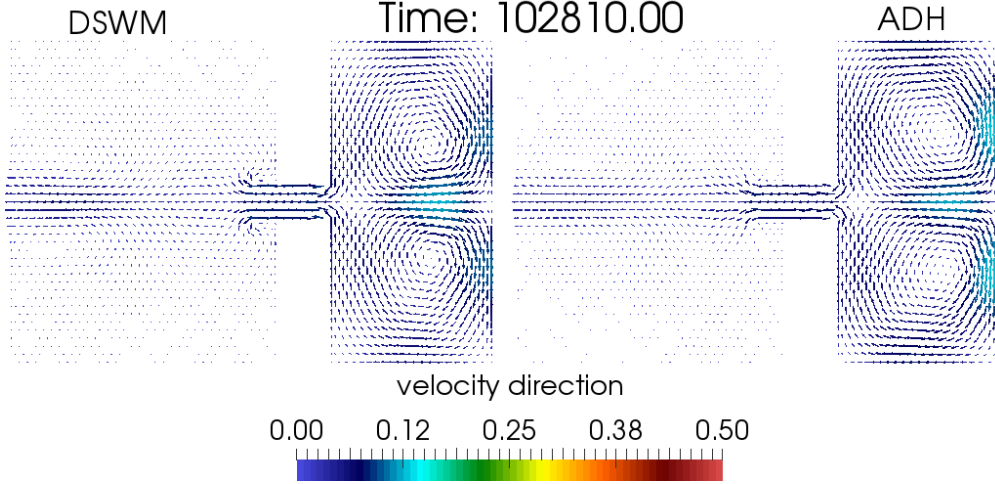


Figure 11: Water velocity field in the idealized inlet test case.

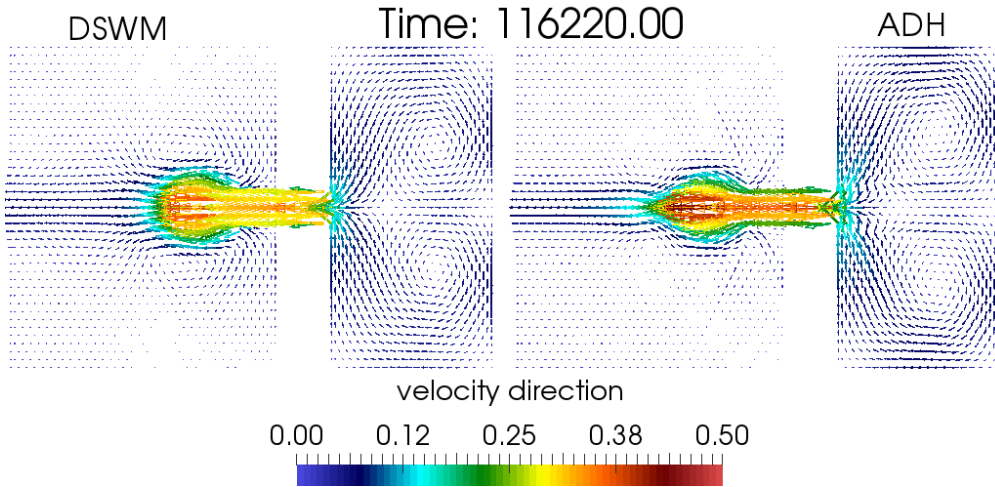


Figure 12: Water velocity field in the idealized inlet test case.

To quantify these localized discrepancies, we provide a comparison of the ADH and our models at two points over time, $(-250m, 0m)$ and $(750m, 0m)$; the first at the boundary of the ebb shoal and the second is at the channel exit. The corresponding plots are shown in Figures 14. In Figure 14, we observe that the ADH model produces a velocity magnitude that is approximately $0.085m/s$ greater than our model. This difference is likely due to the

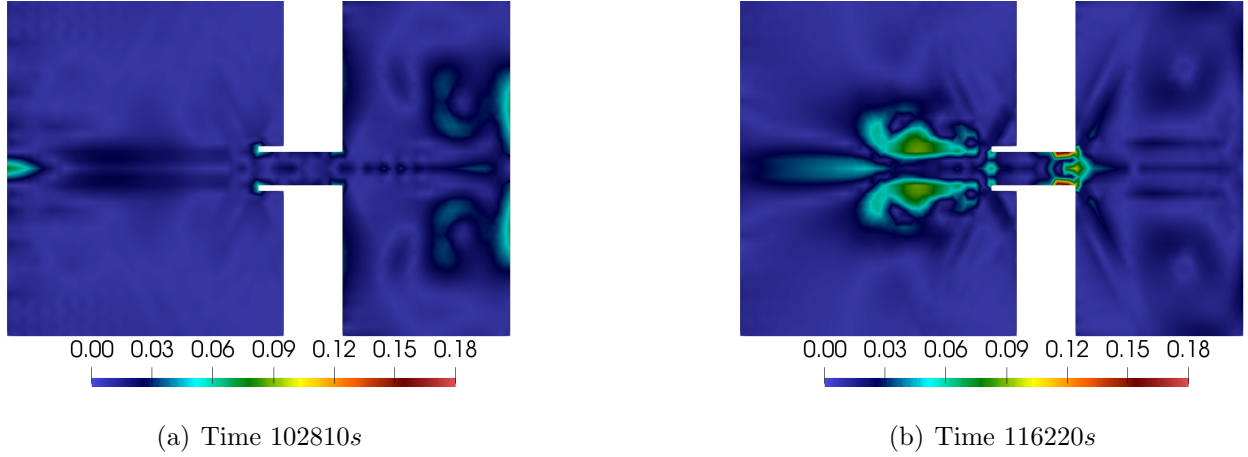


Figure 13: Absolute error of the magnitude of water velocity.

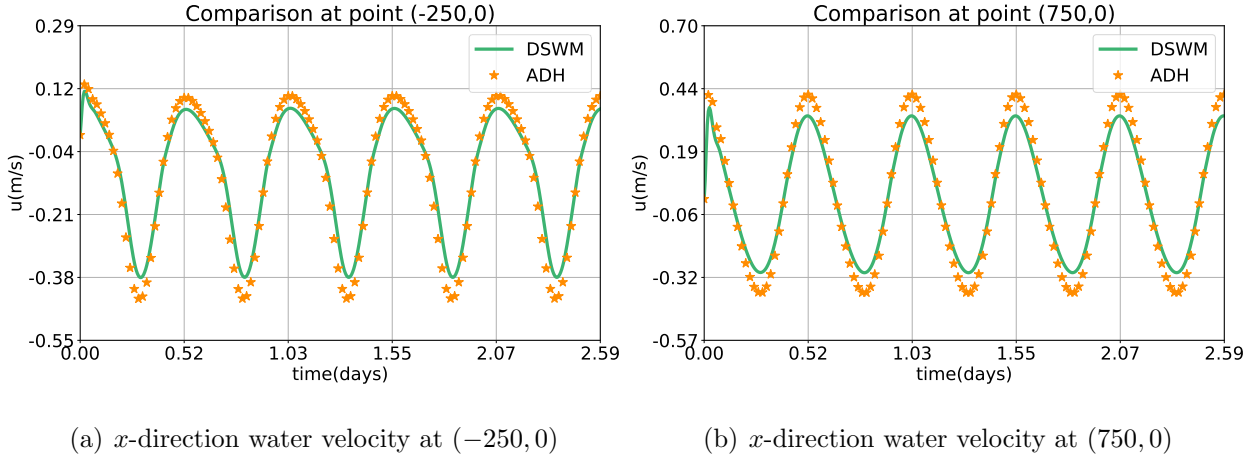


Figure 14: Idealized inlet test case: x -direction velocity.

different approximation schemes in the two models. Since the models share the same periods and trends, we consider this discrepancy within acceptable tolerance.

On the other hand, the surface elevations shown in Figure 15 are nearly indistinguishable between the two models and differ only about 4cm. A good match can be also observed in a comparison between two models over time, see in Fig.(15). We selected two locations $(-250m, 0m)$ and $(750m, 0m)$ here as the example.

3.2.4. Comparison for a Hurricane Event

As a final verification of the deterministic model, we consider Hurricane Ike. To compare our deterministic model to ADCIRC, we select two time steps near the hurricane landfall on

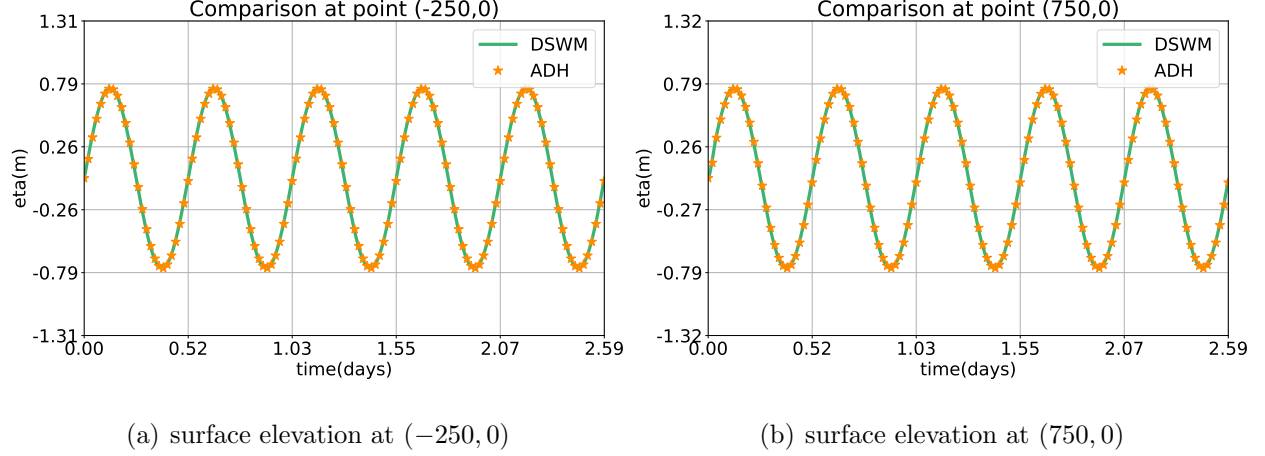


Figure 15: Idealized inlet test case: Surface elevation.

the Texas coast. In Figures 16 and 17, the surface elevation and difference in surface elevation between the two models are shown, respectively. The results show good agreement in the maximum surge near Houston and the maximum absolute difference is $0.5m$ throughout the simulation. In the thesis [22], further comparisons for the deterministic model are included and we refer interested readers to it.

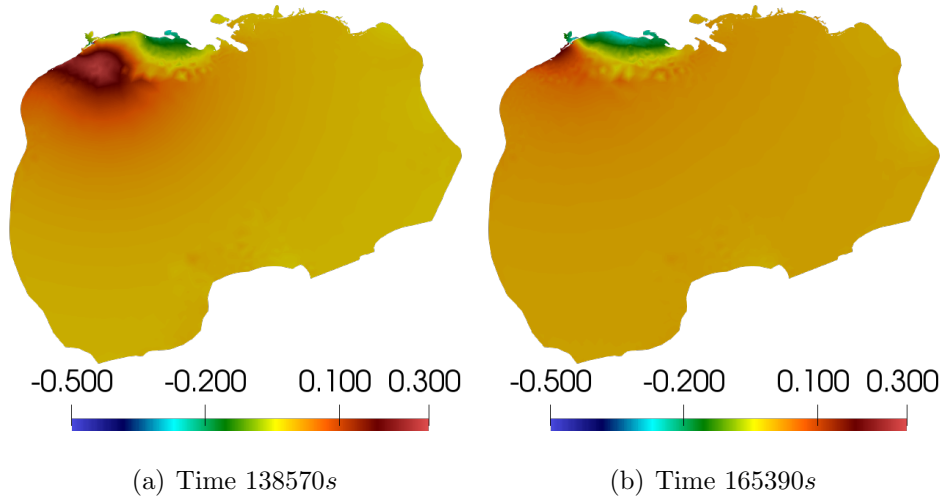


Figure 17: Difference in surface elevation during Hurricane Ike 2008.

3.3. Verification of the SSWM

To verify the full SSWM, we will examine several different uncertain sources as introduced in Section 2.2 one by one: uncertain initial condition, bathymetry, boundary condition, and

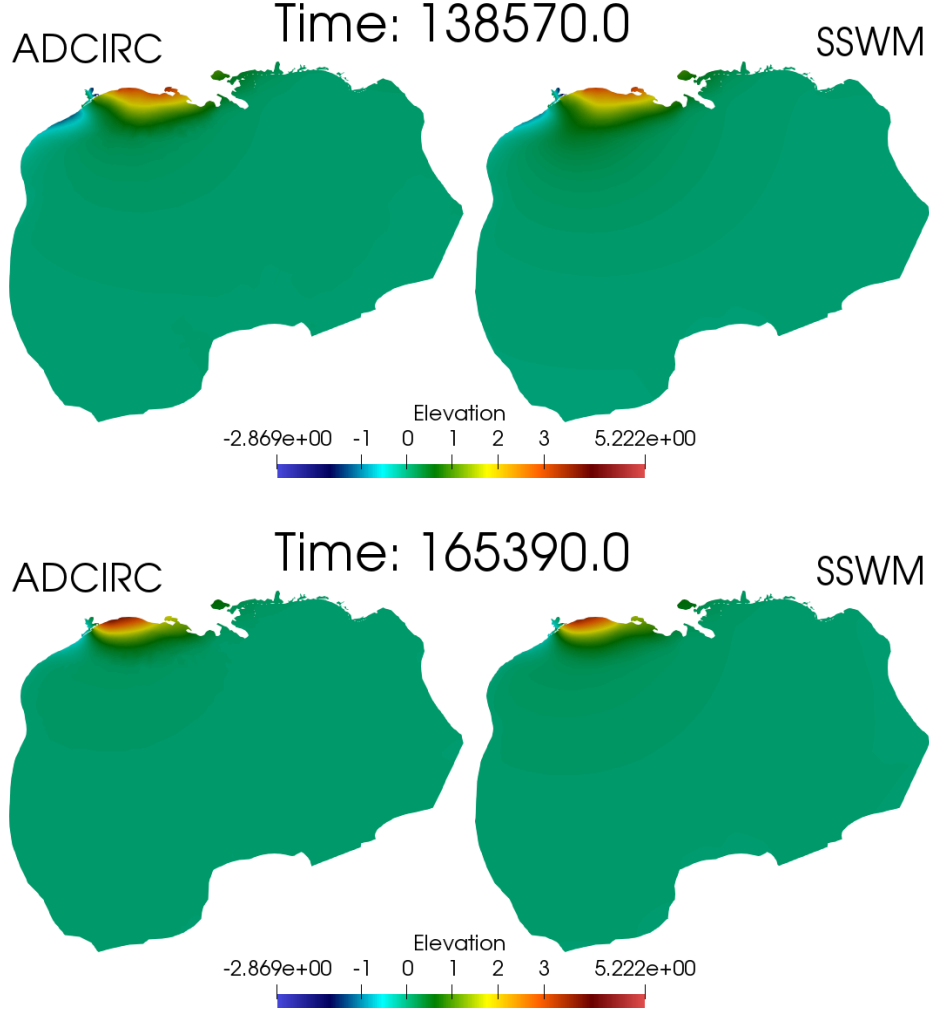


Figure 16: Surface elevation comparisons during Hurricane Ike 2008.

model parameter, i.e., wind drag coefficient. To accomplish such a verification, we note that the output of the SSWM at each spatiotemporal point is indeed a surrogate function which connects model quantities (e.g., surface elevation) to the input random vector ξ . To verify such surrogate functions, we shall perform pointwise comparisons of the surrogate at each sample grid (i.e., the grid within the support of the random vector ξ) in probability space to the value given by each of the corresponding deterministic realizations. Note that this type of comparison process is similar to conducting Monte Carlo experiments. Since we in the previous subsection verified the deterministic part of the SSWM, we trust this DSWM as a verification tool for conducting deterministic realizations. By considering the outputs of the DSWM as benchmarks, we can compute DSWM solutions using the distributed samples

of uncertain model inputs. We subsequently verify the solution function of the SSWM by comparing it pointwise with the collection of results from the DSWM.

3.3.1. Uncertain Initial Condition - Slosh Test Case

In the slosh test case, the uncertain initial condition is $\eta = 0.1\xi_1\xi_2 \cos(\pi x/100.0)$, where ξ_1, ξ_2 are both uniformly distributed given as $\xi_1 \sim U(0.8, 1.2), \xi_2 \sim U(1.0, 2.0)$. We further uniformly sample ξ_1 and ξ_2 to obtain 20 grids each, i.e., 400 sample grids in the random space. Each sample grid is substituted into the full stochastic model and the resulting deterministic model is computed for each sample point. We compare this surrogate against each of the 400 benchmarks and for brevity select only one spatial point $(25.0m, 25.0m)$ to conduct the comparison over its random space. In Figure 18, we observe good agreement for the surface elevation and x velocity component in the top two plots of Figure 18, where color in the background and color in the dot represent quantities given by surrogate and given by benchmark, respectively. In the absolute error map in the two bottom plots of Figure 18, we see the absolute errors in the range of 10^{-4} to 10^{-5} . Finally, we plot the surrogate and benchmark at the spatial point $(25.0m, 25.0m)$ and two sample points $(0.8, 1.0), (1.2, 2.0)$ over all time steps in Figure 19, where we observe good agreement for both surface elevation and x velocity component.

3.3.2. Uncertain Bathymetry - Hump Test Case

In the hump test case, for the uncertain bathymetry given in (25), we again uniformly sample ξ_1 and ξ_2 into 20 grids to obtain 400 sample grids in random space. The spatial point we choose here is $(500.0m, 100.0m)$ and we present a comparison for both surface elevation and x velocity component over the random space at time $t = 155s$ in Figure 21. Here, we observe good match between the surrogate and benchmark over the random space for both surface elevation and x direction water velocity. The last comparison we present in this test case is a time series comparison of the surface elevation and x component of the velocity field at the spatial points $(250.0m, 100.0m)$ and $(750.0m, 100.0m)$ and two sample points $(0.8, 0.9)$ and $(1.2, 1.1)$. This comparison is in Figure 22, where we observe good agreement with the benchmark Monte Carlo solution. The agreement is near perfect in most of the simulation with an exception near the final time. We attribute this discrepancy to accumulation of time

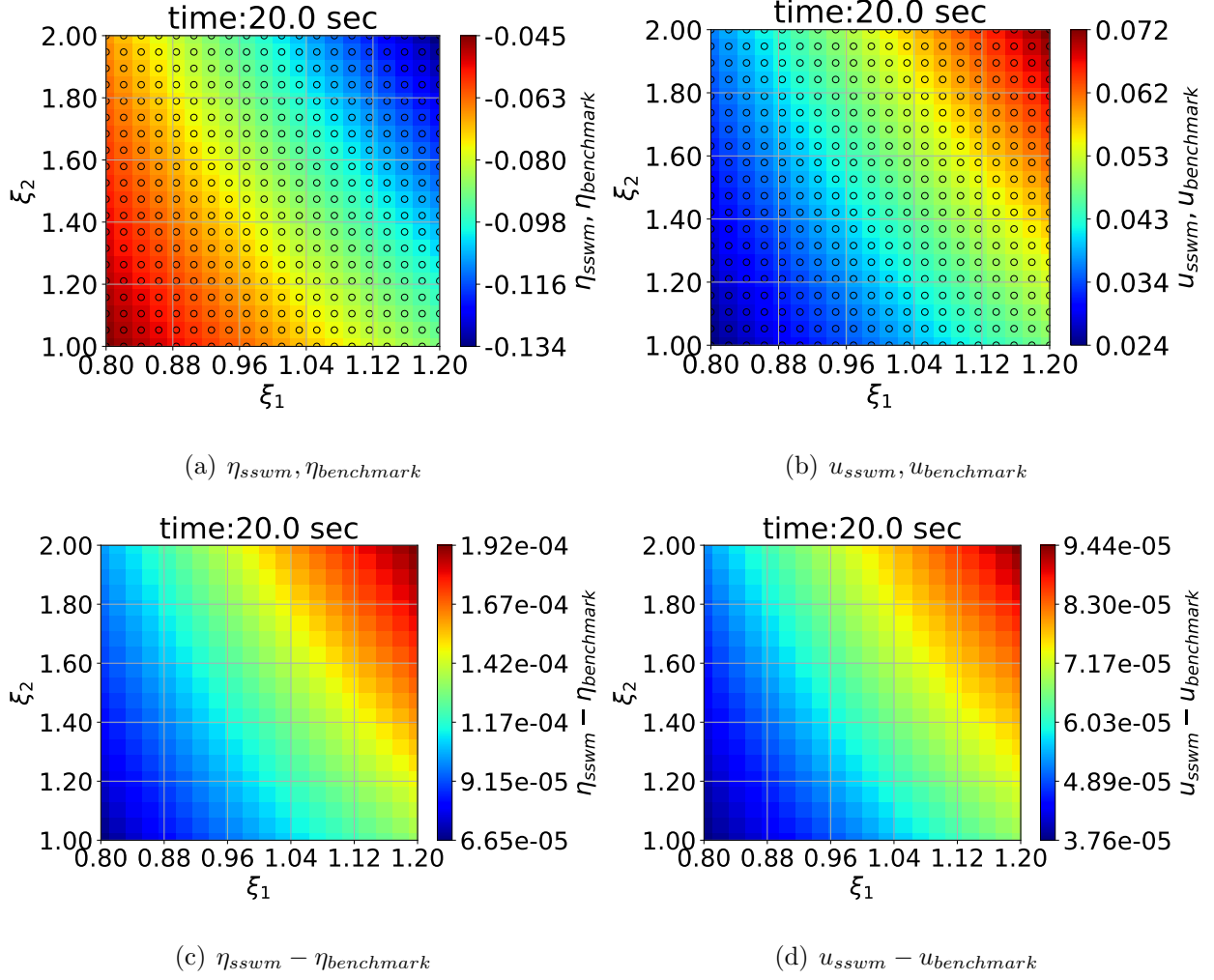


Figure 18: Elevation surrogate comparison at the spatial point (25.0m, 25.0m).

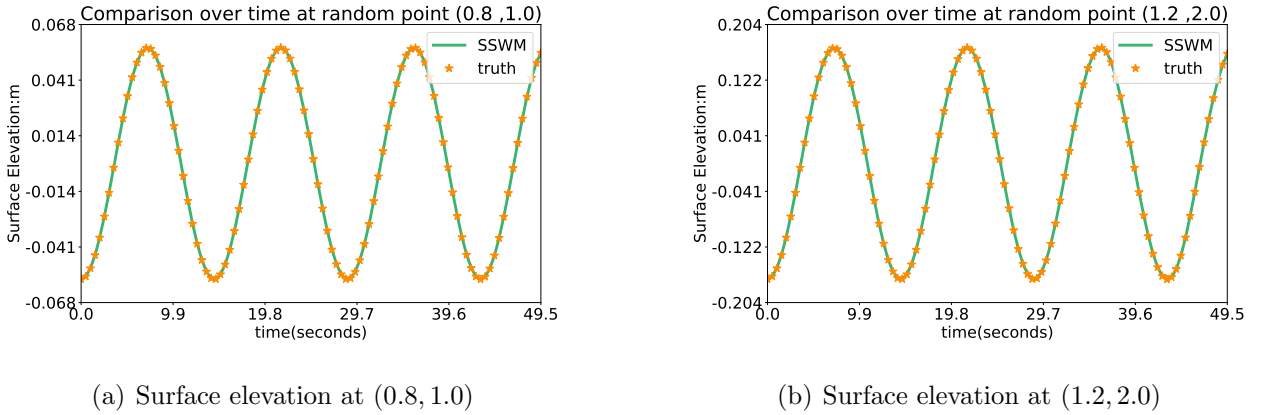


Figure 19: Elevation surrogate and x -direction velocity surrogate compared at a spatial point.

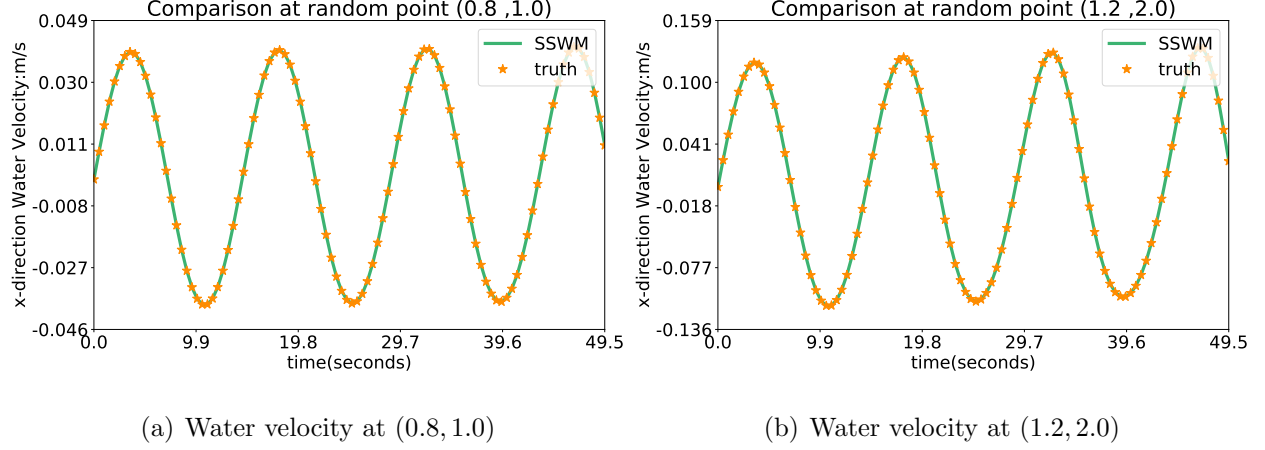


Figure 20: Elevation surrogate and x -direction velocity surrogate compared at a spatial point.

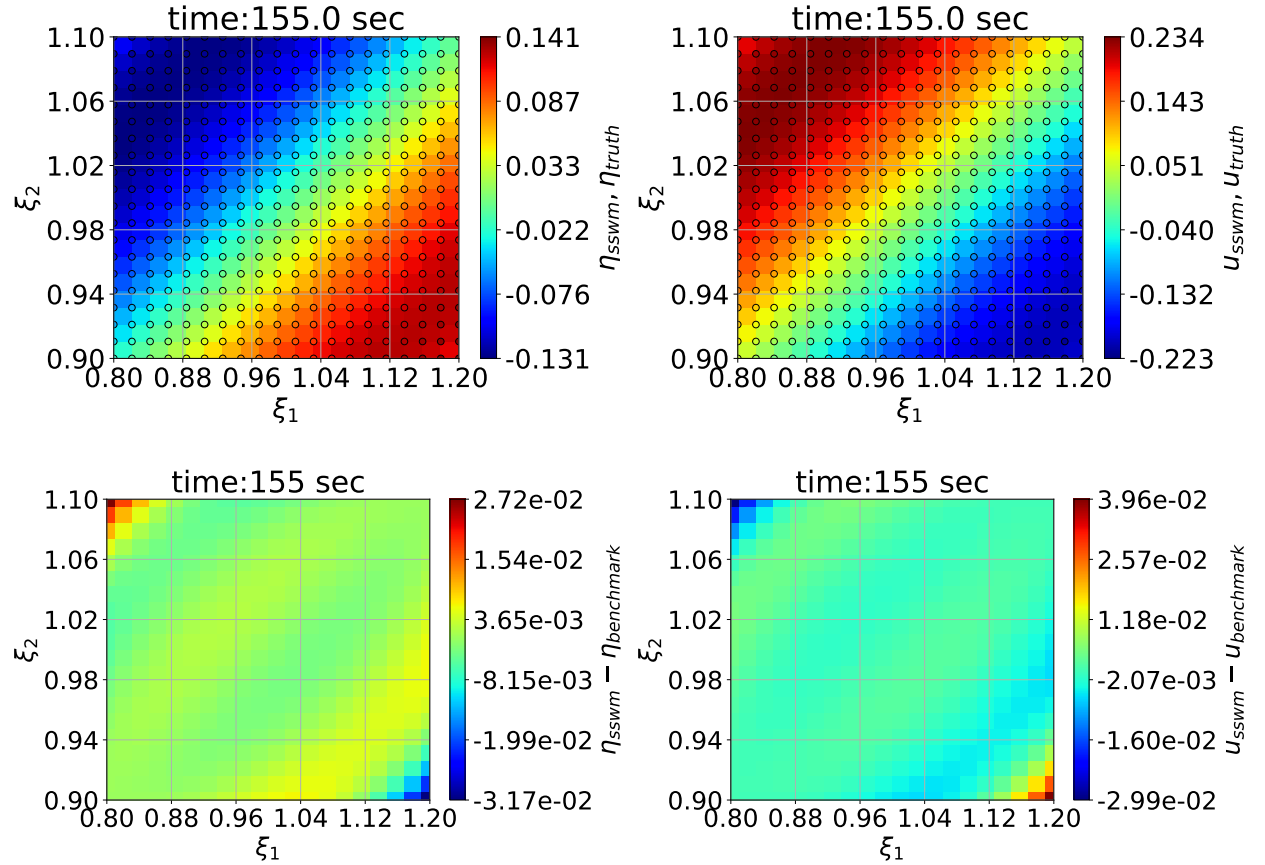


Figure 21: Elevation and velocity surrogate at (500.0m, 100.0m) and time $t = 155$ s.

discretization error. Fortunately, since the phase, amplitude and frequency in both models are nearly identical at the previous time steps, we conclude that the surrogate function can

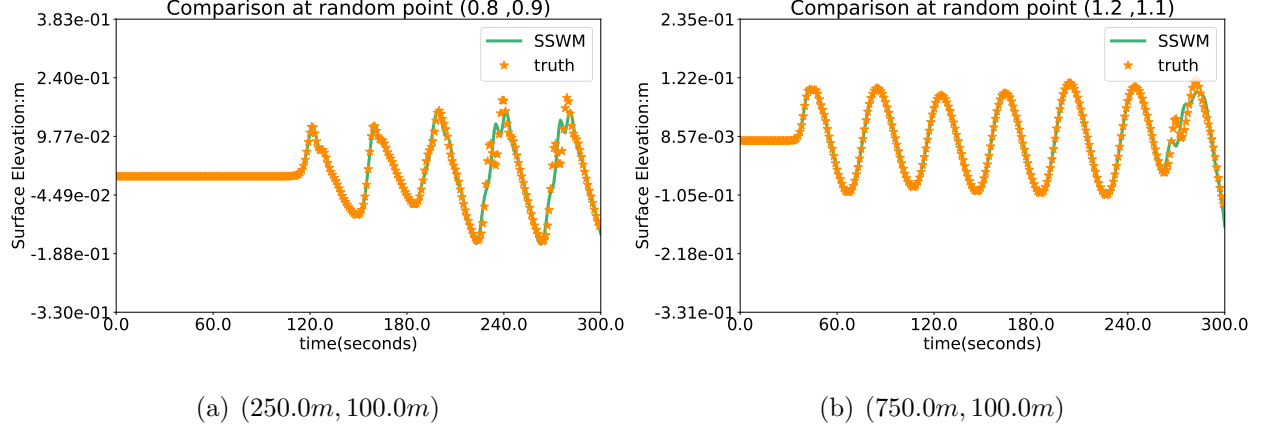


Figure 22: Elevation and velocity surrogate at different spatial and sample points.

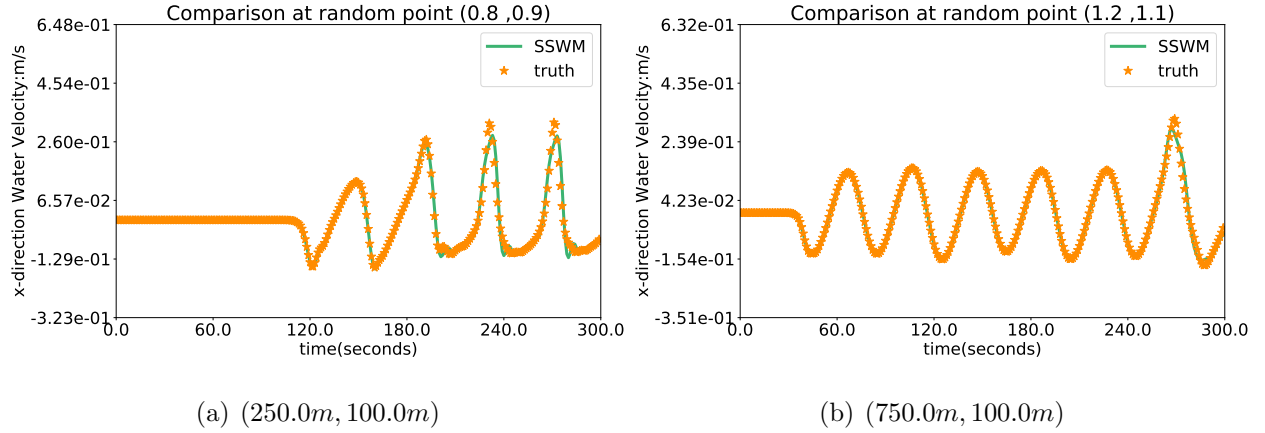
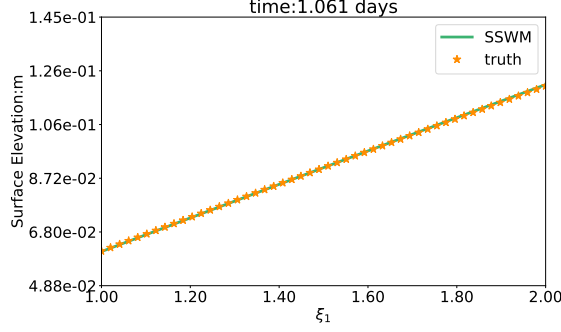


Figure 23: Elevation and velocity surrogate at different spatial and sample points.

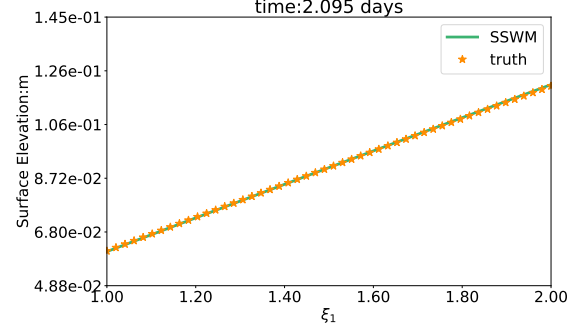
well represent the random space.

3.3.3. Uncertain Boundary Condition - Inlet Test Case

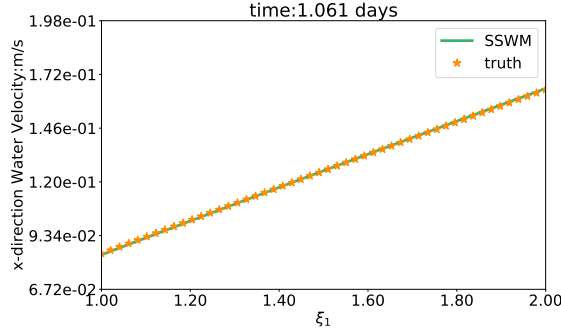
In the inlet test case, we uniformly sample ξ_1 into 50 pieces from the uncertain boundary condition. We compare our surrogate against the 50 benchmarks obtained from running the deterministic model at the corresponding samples. The spatial point of interest is $(0.0m, 0.0m)$, which is located at the entrance of the channel, see Figure 6, and we select two time steps, at 1.061 and 2.095 days, respectively. In Figure 24, we compare the surrogate and the benchmark at the spatial point for all ξ_1 . For the selected times, we observe near perfect agreement in the overall probability space for both surface elevation and x -direction velocity. Next, we consider the temporal distribution of surface elevation and velocity at



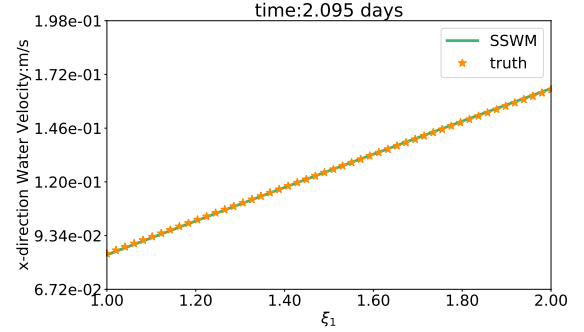
(a) Elevation surrogate at 1.061 days



(b) Elevation surrogate at 2.055 days



(c) x -velocity surrogate at 1.061 days



(d) x -velocity surrogate at 2.055 days

Figure 24: Elevation surrogate at the spatial point $(0.0m, 0.0m)$ over the random space.

$(-250.0m, 0.0m)$. Two sample grids are selected in order to draw a general conclusion: we select the minimum and maximum samples, i.e., $\xi_1 = 1.0, 2.0$ and present the results in Figure 25. Here, the close agreement between the two models is again apparent.

3.3.4. Uncertain Wind Drag Parameter - Hurricane Harvey Test Case

As a final verification of the SSWM, we consider the Hurricane Harvey test case. We again uniformly sample ξ_1 for the uncertain wind drag parameter and compare the resulting surrogate against the 50 benchmarks obtained from running the deterministic model at those corresponding samples. We select a spatial point located at the entrance of the Galveston Bay Channel with longitude and latitude $(-95.24^\circ, 28.85^\circ)$, and two time steps $t = 1.319$ days and $t = 4.139$ days. We present the comparison of elevation, x -velocity, and y -velocity over the random space with respect to ξ_1 in Figure 26. The surface elevation agrees very well in the random space and we only observe minor discrepancies for both velocity components

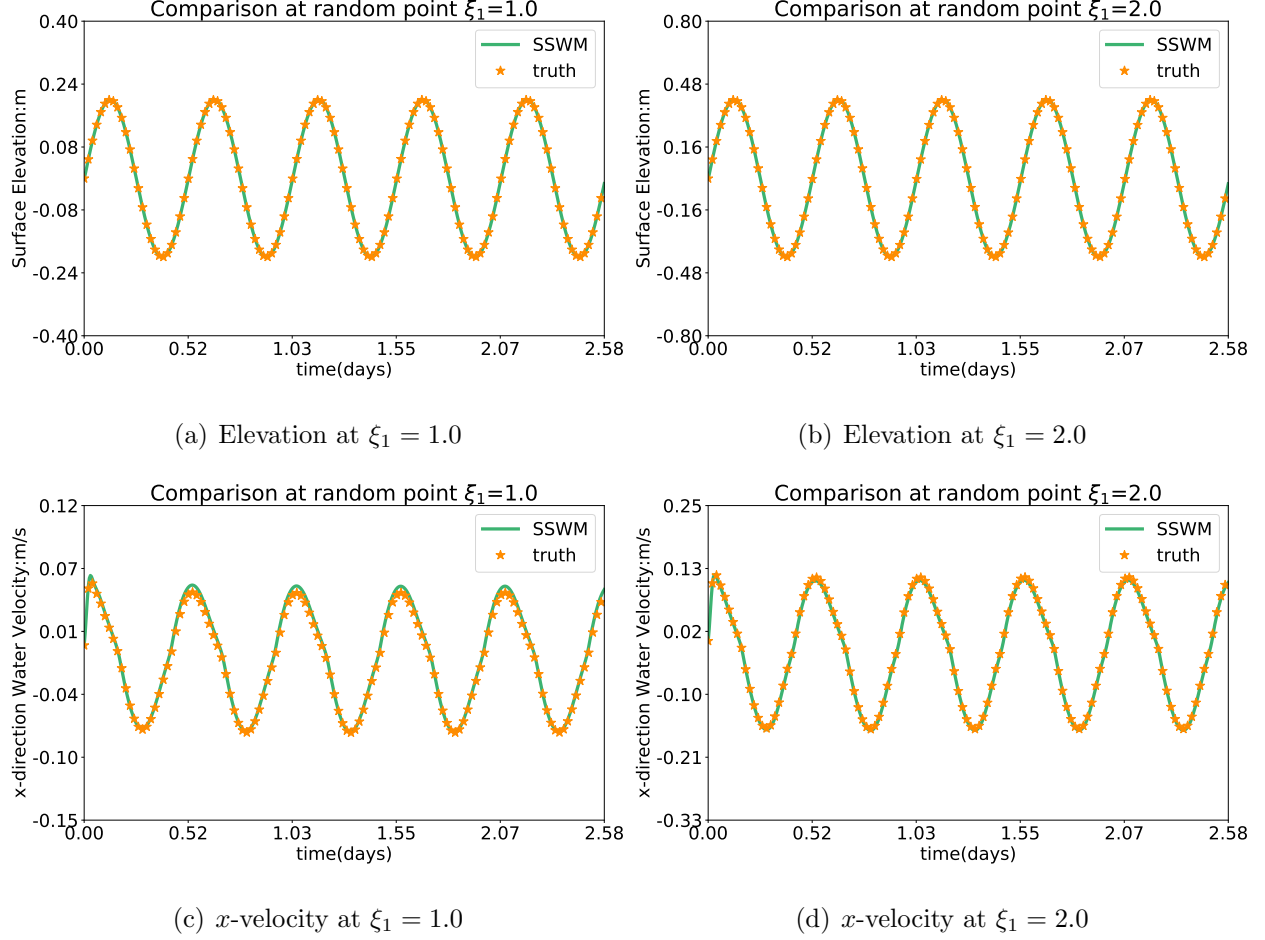


Figure 25: Uncertain boundary condition in the inlet test: Elevation surrogate at the spatial point $(-250.0m, 0.0m)$.

in this figure. Lastly, we consider surface elevation and water velocity against time t at three spatial points $(-95.24^\circ, 28.85^\circ)$, $(-94.51^\circ, 29.43^\circ)$, and $(-94.72^\circ, 29.34^\circ)$. In Figure 27, we present the comparisons of our surrogate and the benchmark. In this figure, we see very close agreement with a small discrepancy in the x velocity component which occurs at approximately five days.

3.4. Notes on the SSWM Verification

We have introduced a SSWM and a set of cross-mode stabilization methods applicable to stochastic hyperbolic systems. For this newly developed model, we provide a comprehensive verification process of both its deterministic and stochastic versions. The verification process demonstrates the effectivity of the proposed cross-mode stabilization methods, as well as the

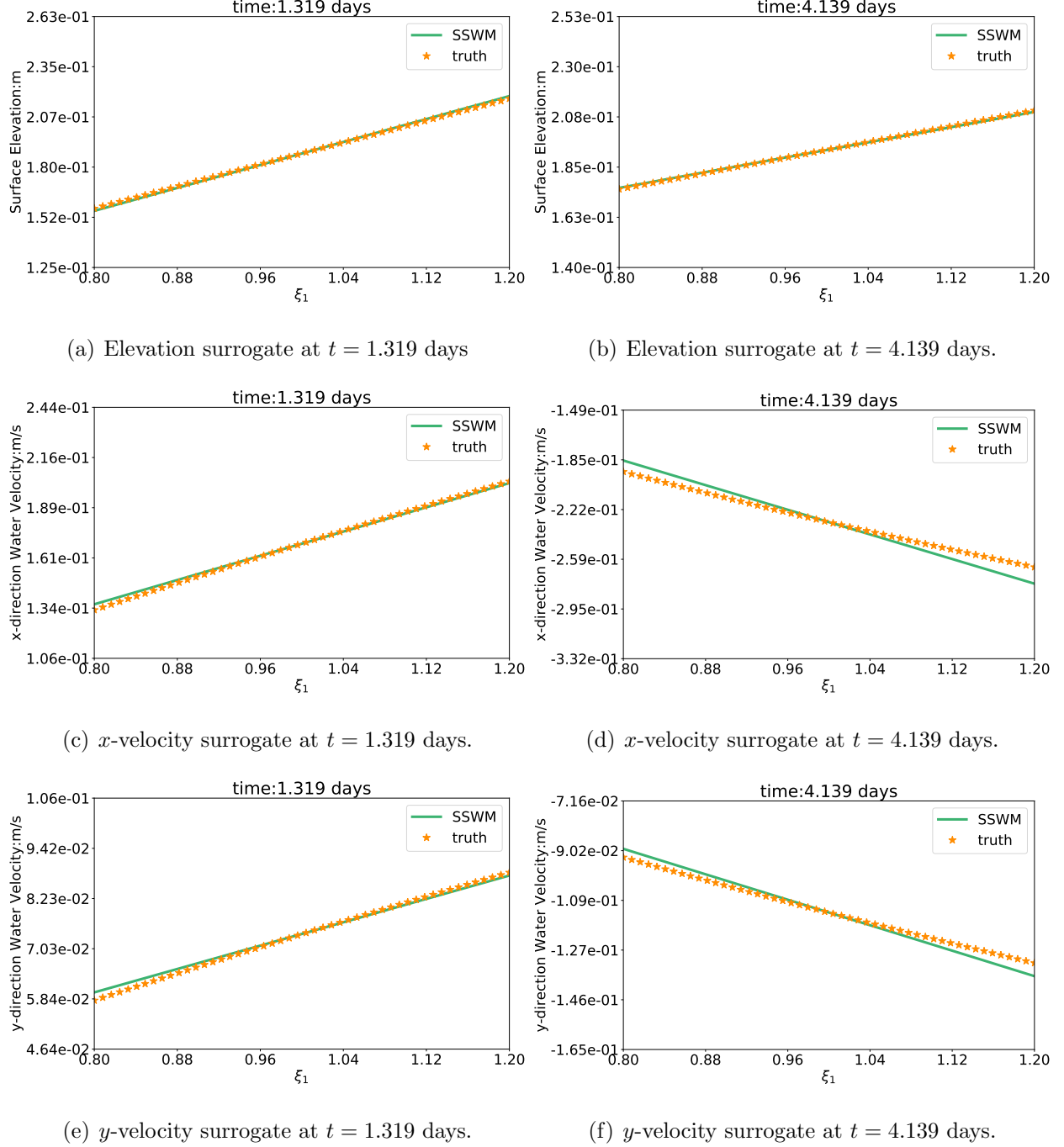


Figure 26: Surrogate comparison for Hurricane Harvey

correctness of the stochastic model. For both ideal and larger physically relevant test cases, we observe good agreement for the proposed SSWM and only small discrepancies in some cases. This indicates that the approximations made in the SSWM do not deteriorate the solution, i.e., the computed surrogates. Hence, we conclude that the stochastic model is

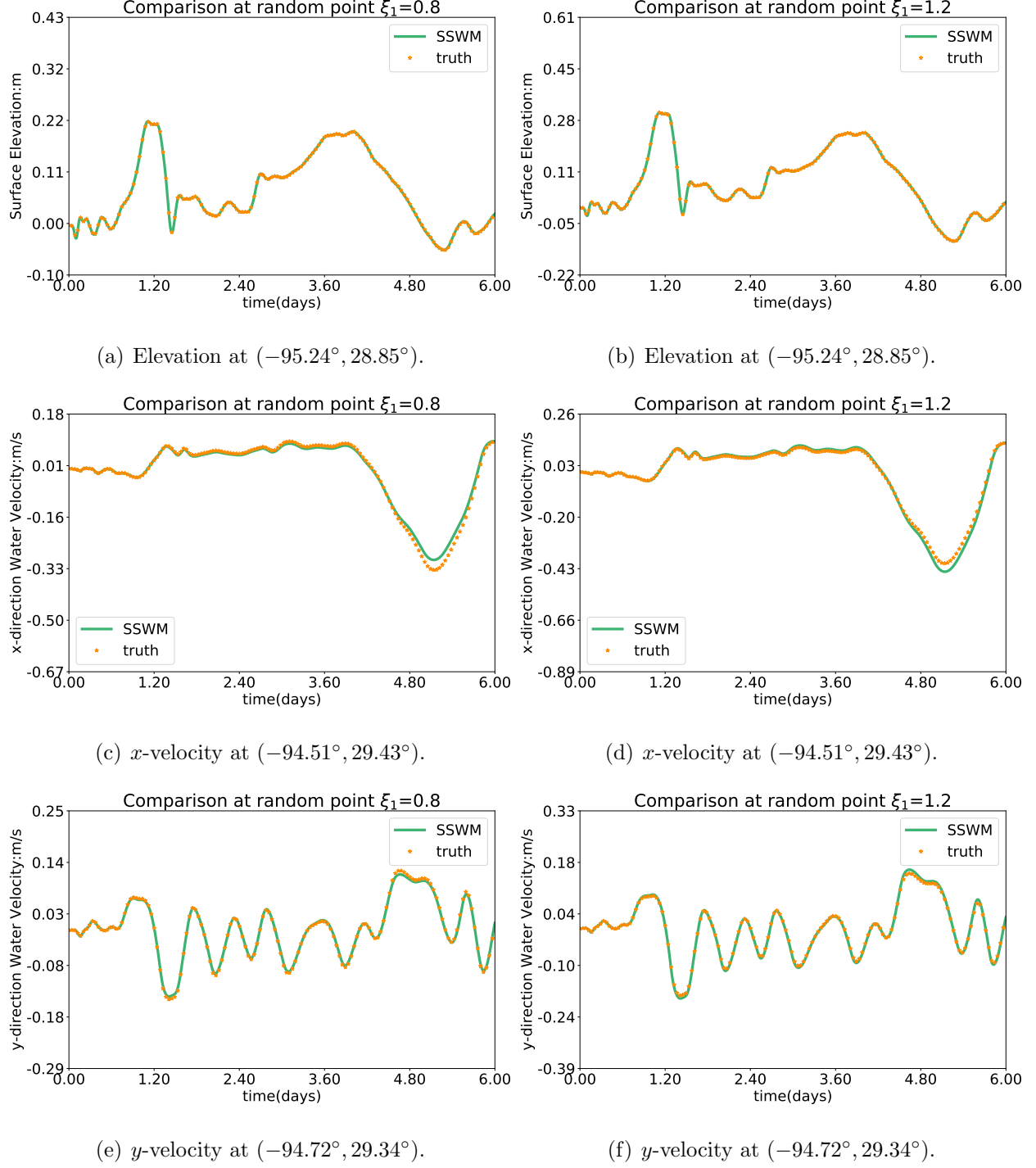


Figure 27: Time series surrogate comparison at three spatial points.

verified and capable to produce reliable surrogates for the further statistical analysis. In the following two sections, we validate the SSWM through a detailed statistical analysis as well as hindcasting of the two considered hurricanes.

4. Visualization and Analysis of the Second-Order Stochastic Process

In this section, we will explore the underlying properties of the stochastic process utilizing the numerical tests introduced in Section 3.1. In each of the following three subsections we investigate the magnitude of the variance of the model outputs, the PDF, and the maximum variance magnitude, respectively.

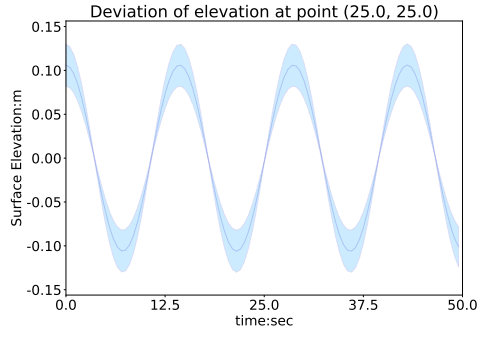
4.1. The Variation of Variance

Based on the verification of our SSWM in Section 3, we can now use it to compute higher order moments of the output random variables. Among the higher-order moments, the second-order central moment, i.e., the variance, is of particular importance. Hence, we will explore the relationship between the variance in the model inputs and the variance in the model outputs as well as what affects the magnitude of the variance in the model outputs.

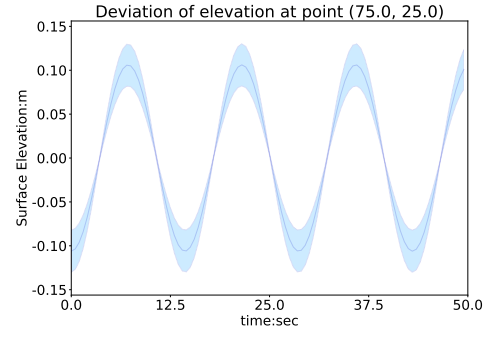
To study the sensitivity of the variance, we consider the slosh test case described in Section 3.1.1, where the uncertain initial condition has the form $\eta = 0.1\xi_1\xi_2 \cos(\pi x/100.0)$, where ξ_1, ξ_2 are uniformly distributed. In this experiment, we fix $\xi_1 \sim U(0.8, 1.2)$ and vary ξ_2 as $U(1.0, 2.0)$, $U(0.5, 2.5)$, and $U(0.25, 2.75)$. We pick two spatial points $(25.0m, 25.0m)$ and $(75.0m, 25.0m)$ to show the variation of variance in the surface elevation and x component of water velocity in Figures 28 and 29, respectively. In both figures, the blue shaded area corresponds to one standard deviation at that spatial point and the central blue line represents the variation mean of the model solution. We observe in Figures 28 and 29 that the variance in both surface elevation and water velocity increases as the uncertain range of ξ_2 extends. Hence, the variance of the input directly impacts the variance of the output in an intuitive fashion: the variance of output increases as the variance of inputs increase.

4.2. The time-varying probability density function

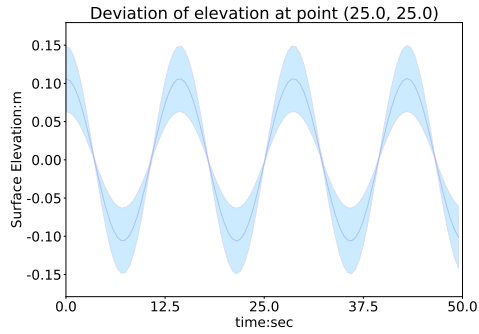
The PDF is often used to define random variables and in this section, we investigate PDFs from the SSWM outputs and the similarities between multiple PDFs in space and time. To visualize the predicted PDF at a fixed point in space and time, we distribute 1000 samples on ξ_1, ξ_2 and collect the sample outputs based on the surrogate response. We subsequently uniformly discretize the range of sample outputs into 30 bins and draw a



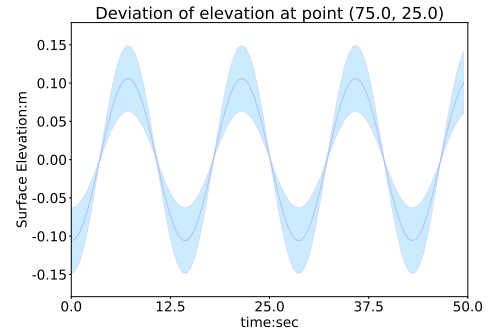
(a) Deviation with $\xi_2 \sim U(1.0, 2.0)$



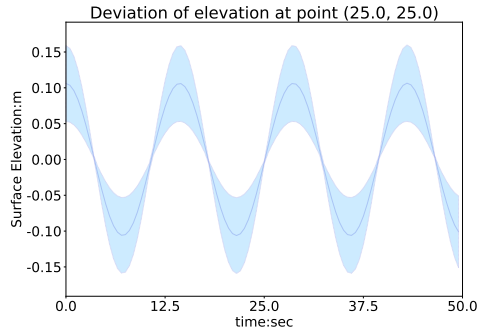
(b) Deviation with $\xi_2 \sim U(1.0, 2.0)$



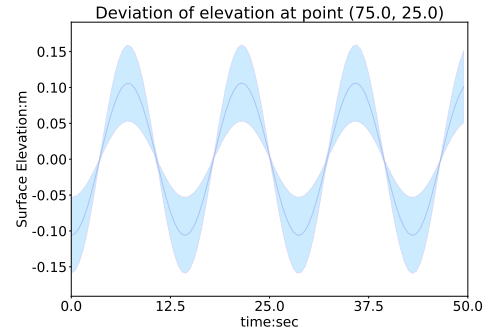
(c) Deviation with $\xi_2 \sim U(0.5, 2.5)$



(d) Deviation with $\xi_2 \sim U(0.5, 2.5)$



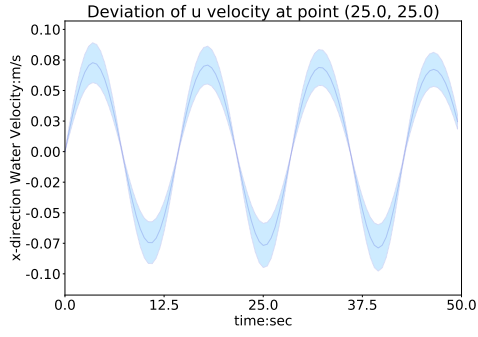
(e) Deviation with $\xi_2 \sim U(0.25, 2.75)$



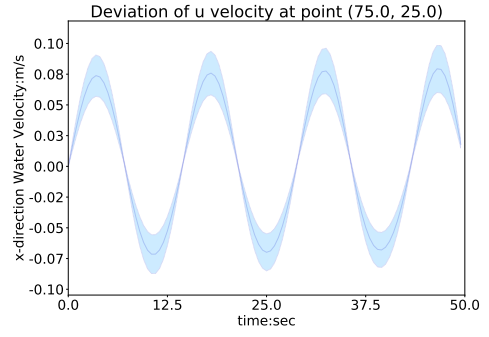
(f) Deviation with $\xi_2 \sim U(0.25, 2.75)$

Figure 28: Deviation of surface elevation at spatial points $(25.0m, 25.0m)$ and $(75.0m, 25.0m)$.

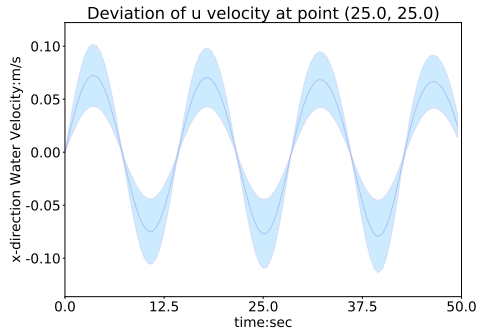
histogram with its kernel-estimated PDF. With a visualized PDF, we visually inspect and investigate similarities among the different output quantities. For each of the ideal test cases introduced in Section 3.1, we ascertain PDFs at selected spatial and temporal locations for analysis. In the histograms presented in the following figures, the light blue shaded area



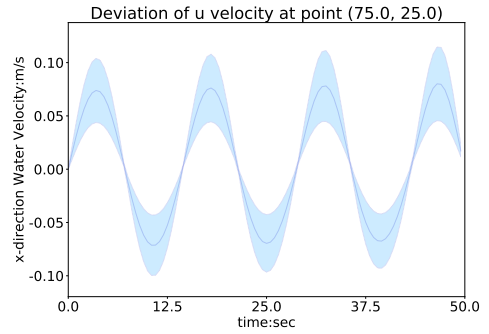
(a) Deviation with $\xi_2 \sim U(1.0, 2.0)$



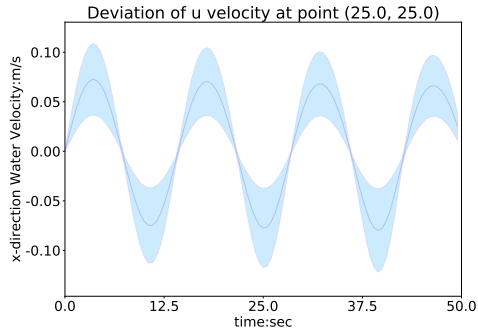
(b) Deviation with $\xi_2 \sim U(1.0, 2.0)$



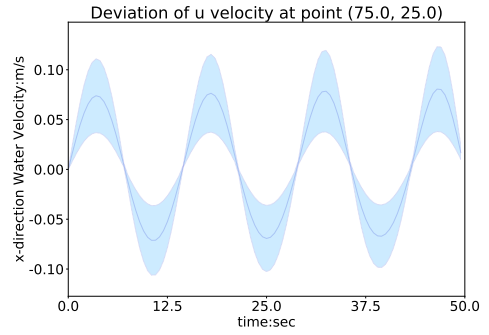
(c) Deviation with $\xi_2 \sim U(0.5, 2.5)$



(d) Deviation with $\xi_2 \sim U(0.5, 2.5)$



(e) Deviation with $\xi_2 \sim U(0.25, 2.75)$



(f) Deviation with $\xi_2 \sim U(0.25, 2.75)$

Figure 29: Deviation of x -direction water velocity at spatial points $(25.0m, 25.0m)$ and $(75.0m, 25.0m)$.

represents the PDF distribution of a random variable and the darker blue line in these plots corresponds to a kernel density estimation of the presented distribution.

4.2.1. Uncertain Bathymetry

Recall that in the hump test case, the bathymetry is uncertain, see (25). Here, we provide PDFs at the points $(250.0m, 100.0m)$ and $(750.0m, 100.0m)$, which are located at one-quarter and three-quarters of the domain, respectively. The PDFs of surface elevation and water velocity at these spatial points at the selected time steps are shown in Figures 30 through 33. Let us first compare the surface elevation and the water velocity PDFs at $(250.0m, 100.0m)$ at time $t = 110s$, i.e., Figure 30(a) and 31(a). Here we observe that the PDFs of both surface elevation and water velocity can be estimated using beta distribution with different shape parameters α and β . In fact, this phenomenon can be observed at all the six time steps, by comparison of the other sub figures in Figure 30 and Figure 31. Furthermore, this trend is also observed at $(750.0m, 100.0m)$ and all six time steps in Figures 32 and 33. Hence, the predicted PDFs between each output quantity (η and \mathbf{u}) at a fixed spatial point at a fixed time are similar. In this test case we note that a beta distribution can be used to estimate the predicted PDF for each output quantity at a fixed spatial point at a fixed time. Second, let us compare the surface elevation PDFs at $(250.0m, 100.0m)$ at each of the selected six time steps, i.e., compare all sub figures in Figure 30. We again observe that the PDFs at these times are similar in the sense that they can be estimated using the same beta distribution with changing parameters. This indicates that the stochastic process for surface elevation at the point $(250.0m, 100.0m)$ can be estimated by a beta distribution with time-varying shape parameters $\alpha(t)$ and $\beta(t)$. This trend is also identical for the x velocity component PDFs at $(250.0m, 100.0m)$ in Figure 31 as well as for the other point in Figures 32, and 33. Thus, at a fixed point, the predicted PDF for both output quantities are similar, i.e., the stochastic process at a fixed spatial point for both output quantities can be estimated by one type of distribution. In particular in this test case, we can use one beta distribution with the time-varying shape parameters $\alpha(t)$ and $\beta(t)$ to describe the stochastic process of η and \mathbf{u} . These observed trends for the selected points are identical for other points in the problem domain (omitted here for brevity, see [22]), and can be generalized to the entire physical space. Hence, one beta distribution with space-time varying parameters $\alpha(\mathbf{x}, t)$ and $\beta(\mathbf{x}, t)$ can be used to describe the stochastic processes for each output quantity η and \mathbf{u} .

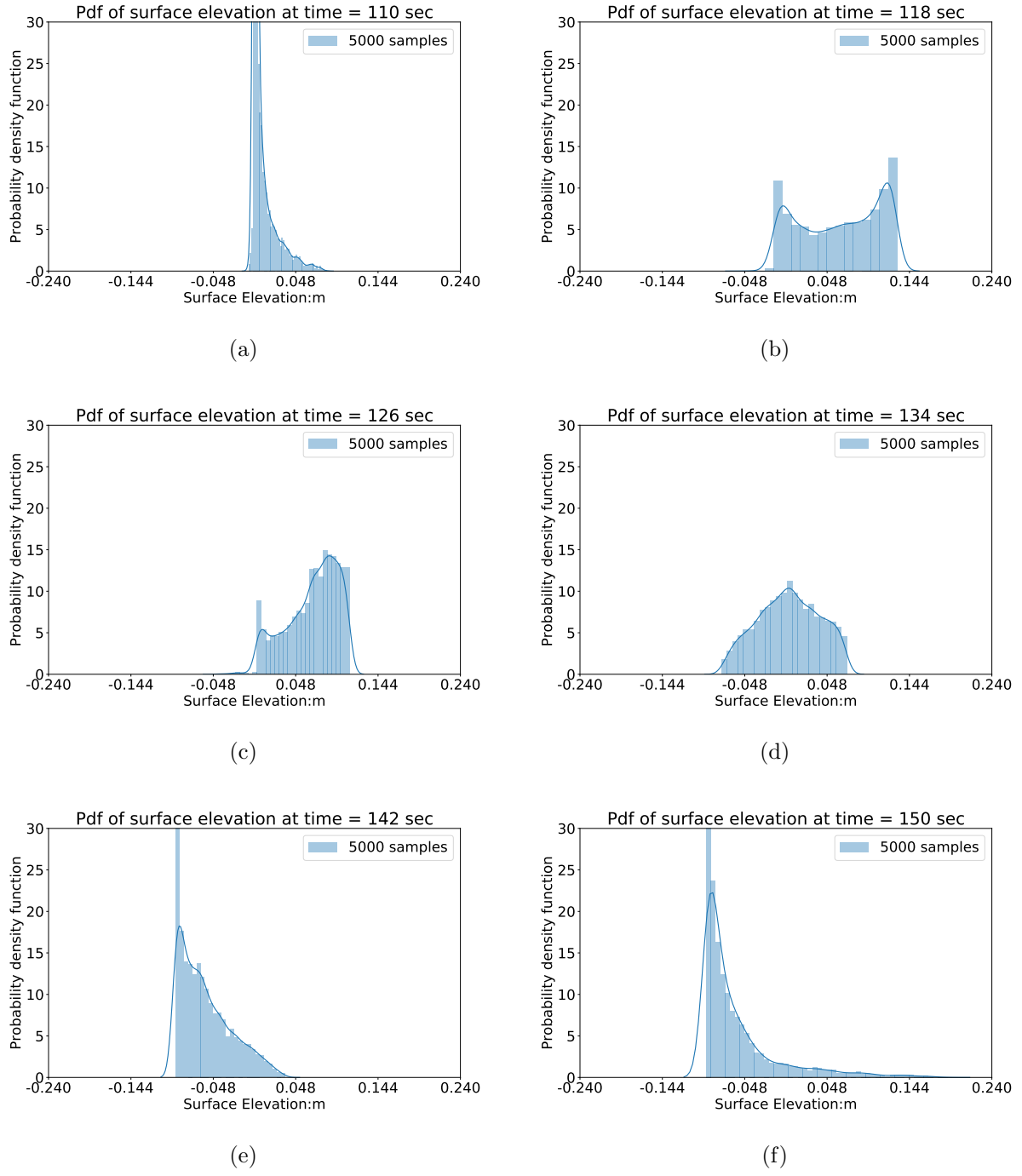
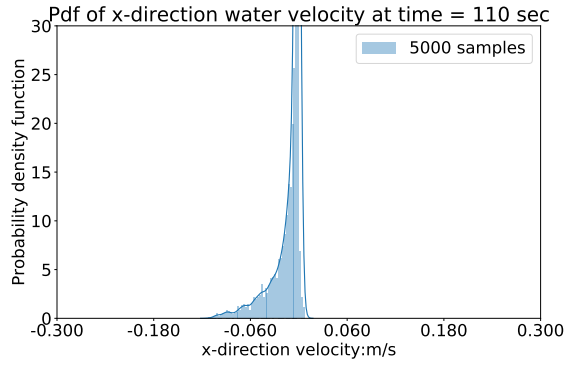
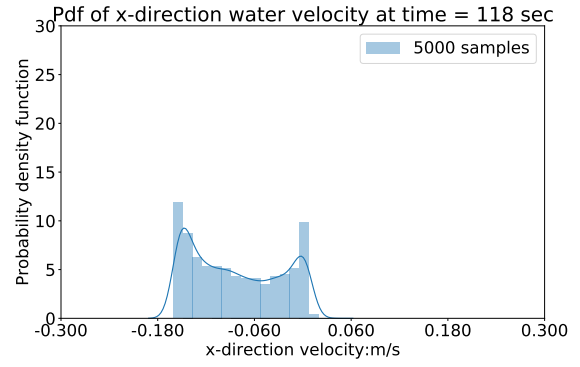


Figure 30: Elevation PDFs at $(250.0m, 100.0m)$.

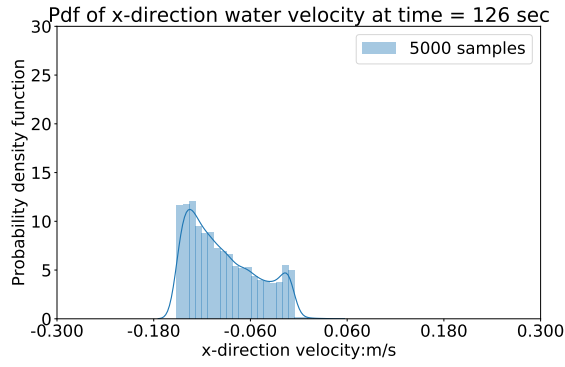
The observed trends in the PDFs are expected due to our use of the same polynomial chaos expansions for both \mathbf{u} and η . As the task of the SSWM is actually to compute the coefficient at each point and time, i.e., $\mathbf{u}_i(\mathbf{x}, t)$ and $\eta_j(\mathbf{x}, t)$, it is expected to observe the



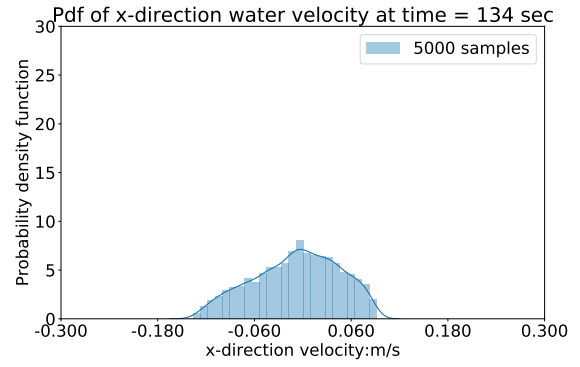
(a)



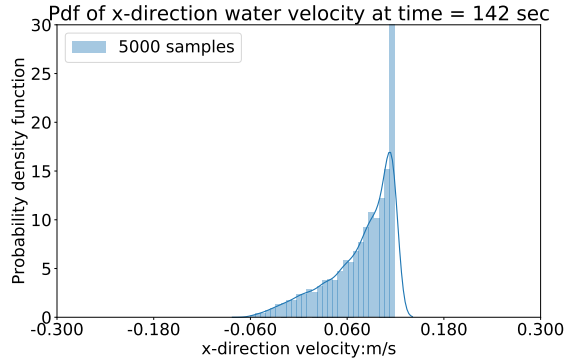
(b)



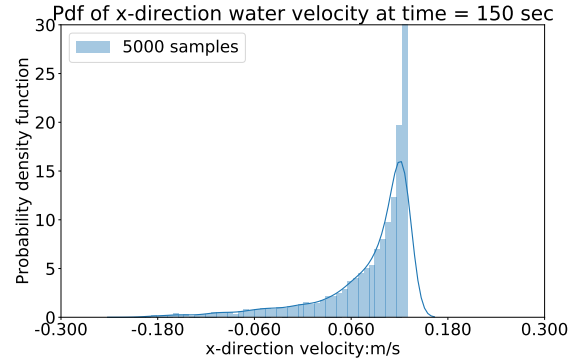
(c)



(d)



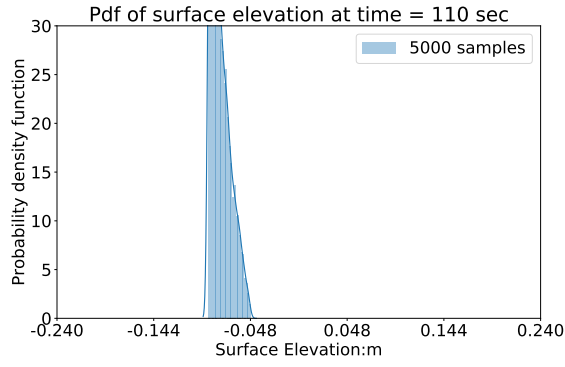
(e)



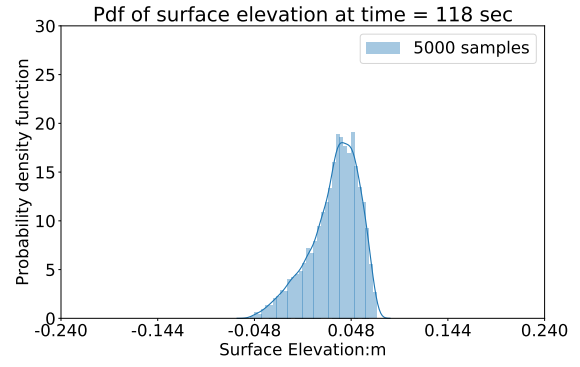
(f)

Figure 31: x direction velocity PDFs at $(250.0m, 100.0m)$.

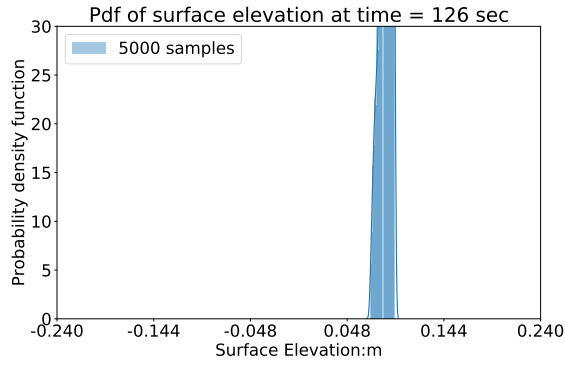
same type of distribution over the domain throughout the simulation time.



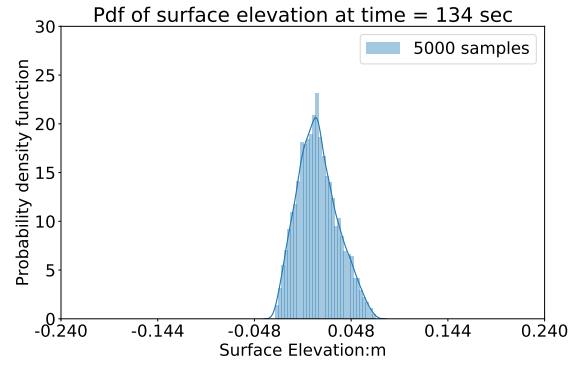
(a)



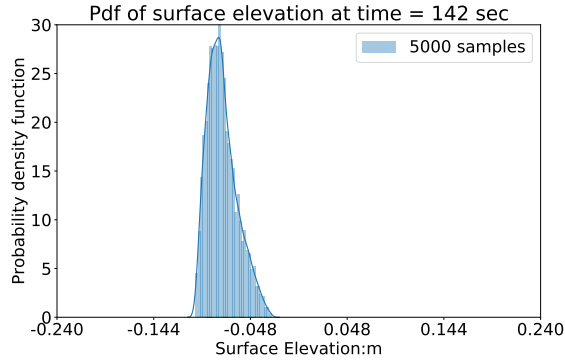
(b)



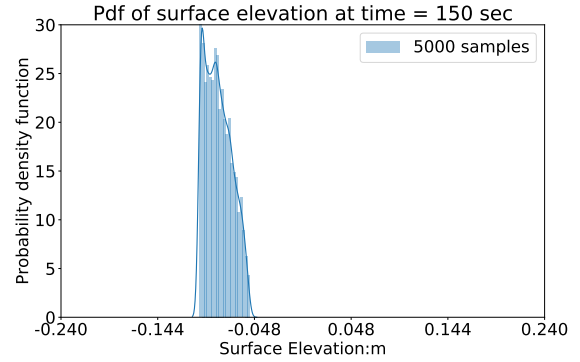
(c)



(d)



(e)

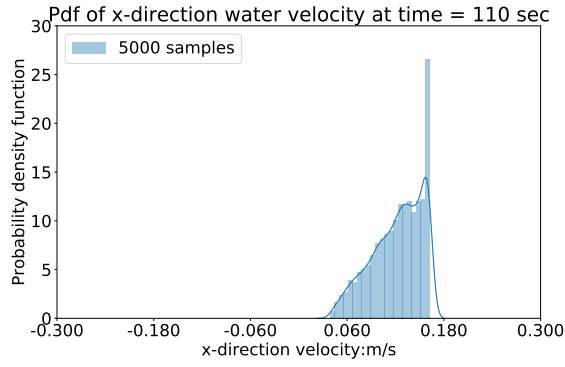


(f)

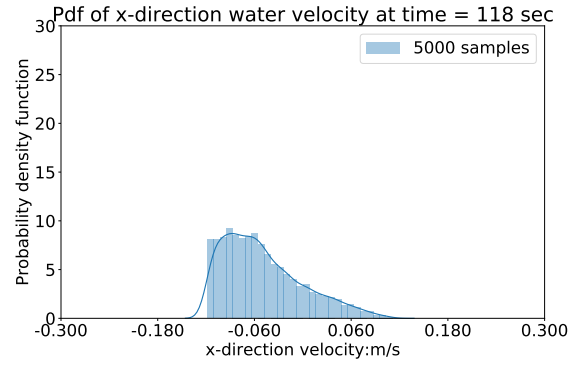
Figure 32: Elevation PDFs at $(750.0m, 100.0m)$.

4.2.2. Uncertain Initial Condition

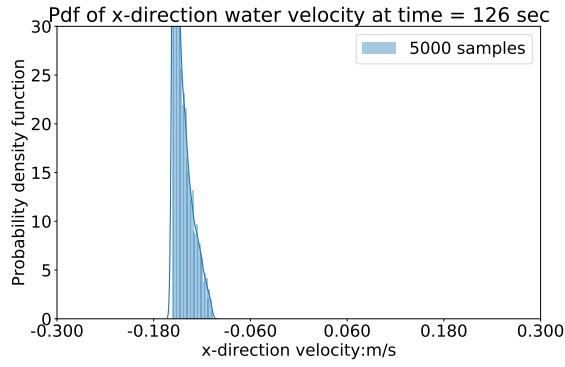
We again consider the slosh test case with an uncertain initial condition, and select a spatial point $(25.0m, 25.0m)$ at which we visualize its predicted PDFs at four specific times.



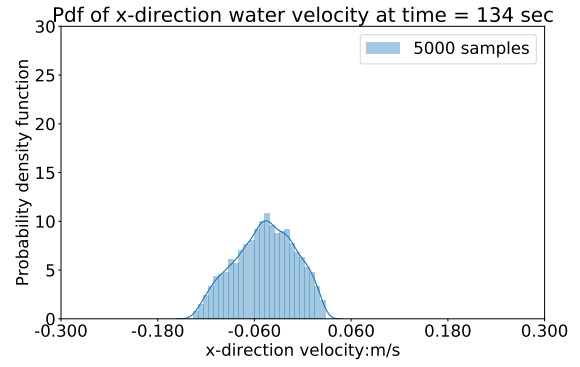
(a)



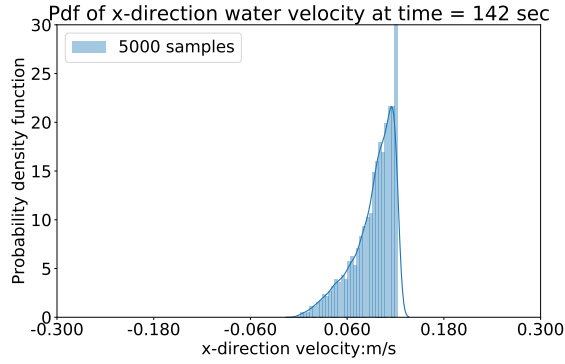
(b)



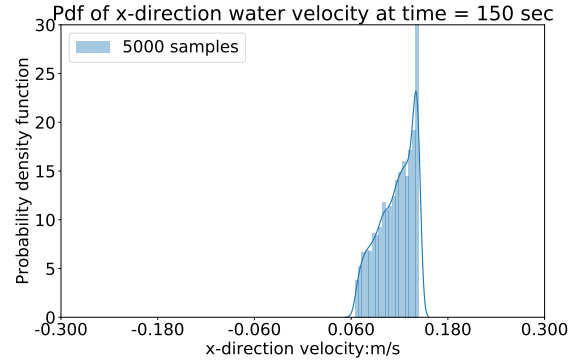
(c)



(d)



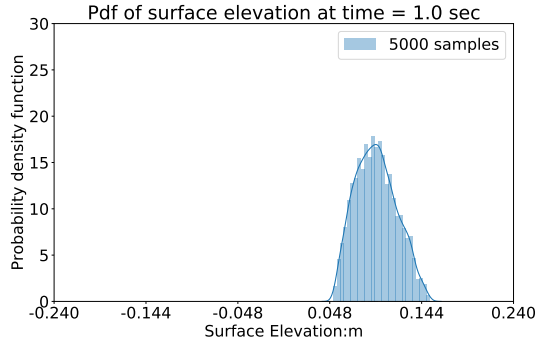
(e)



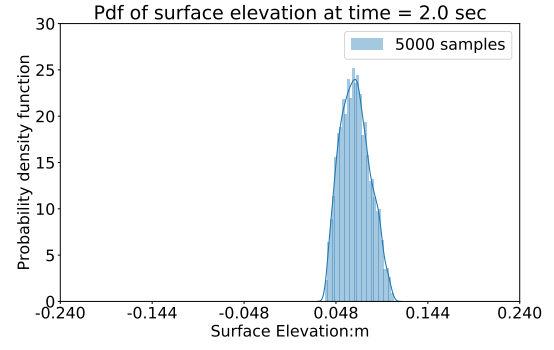
(f)

Figure 33: x direction velocity PDFs at $(250.0m, 100.0m)$.

The PDFs of the surface elevation and the water velocity at that spatial point at the selected time steps are shown in Figures 34, 35, 36, and 37. In this case, these figures reveal that the PDF of both the surface elevation and the water velocity can be estimated using log-normal

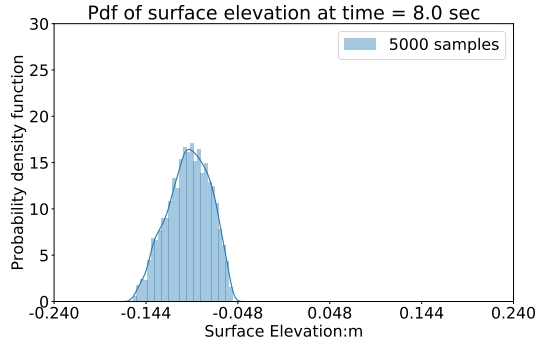


(a)

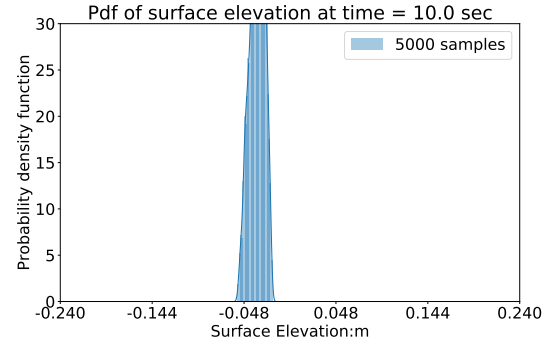


(b)

Figure 34: PDF of the surface elevation at $(25.0m, 25.0m)$.

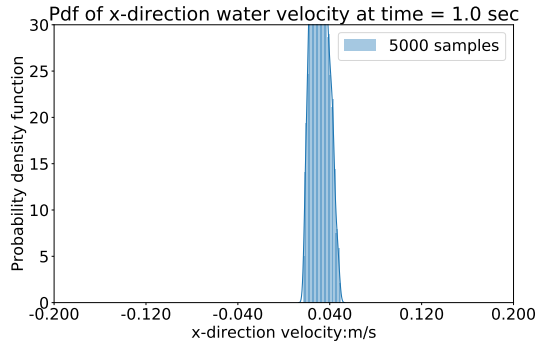


(a)

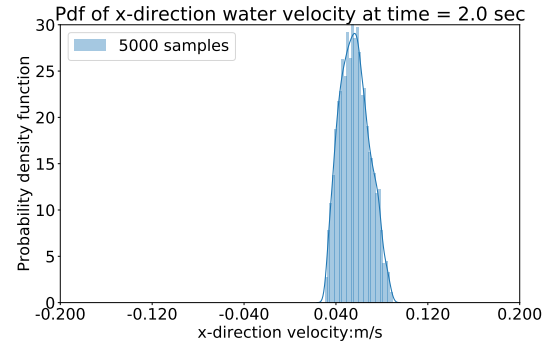


(b)

Figure 35: PDF of the surface elevation at $(25.0m, 25.0m)$.



(a)



(b)

Figure 36: PDF of the x velocity at $(25.0m, 25.0m)$.

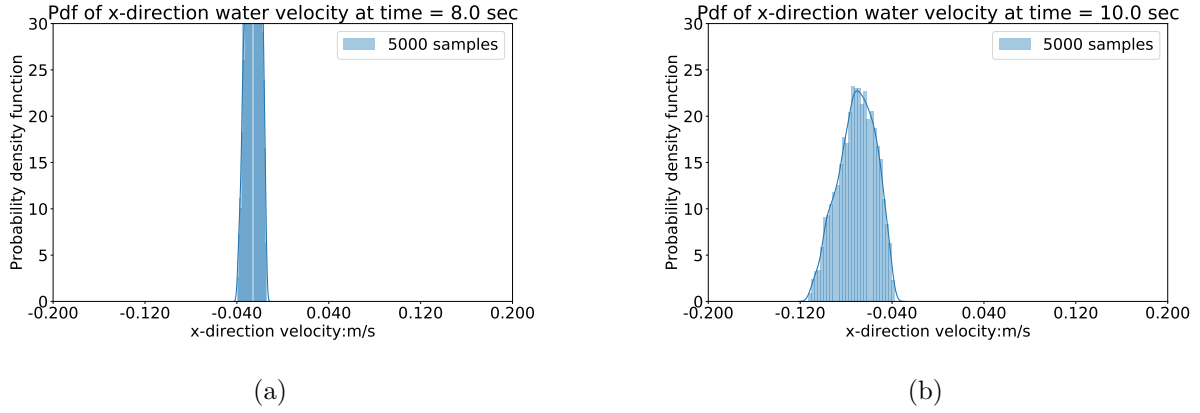


Figure 37: PDF of the x velocity at $(25.0m, 25.0m)$.

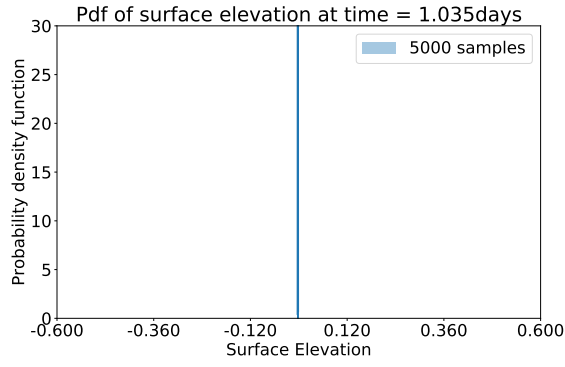
distribution with space-time varying means and variances.

4.2.3. Uncertain Boundary Condition

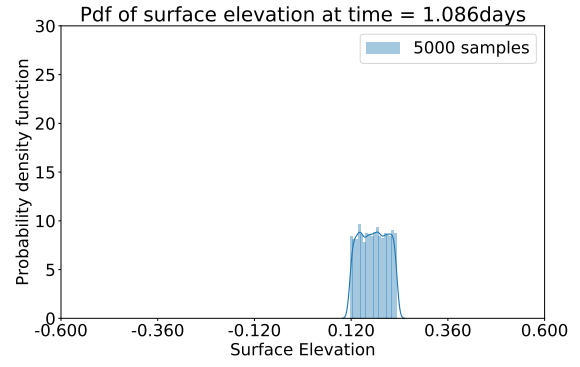
In the inlet test case, the elevation boundary condition represents the uncertain source. In this test case, we choose a spatial point $(0.0m, 0.0m)$ at the entrance of the inlet in the domain and present the PDFs of the surface elevation and the water velocity at six times in Figures 38 and 39. In this case, the PDFs resembles uniform distributions that can be described with space-time varying intervals for both the surface elevation and the water velocity.

4.2.4. Notes on the PDFs

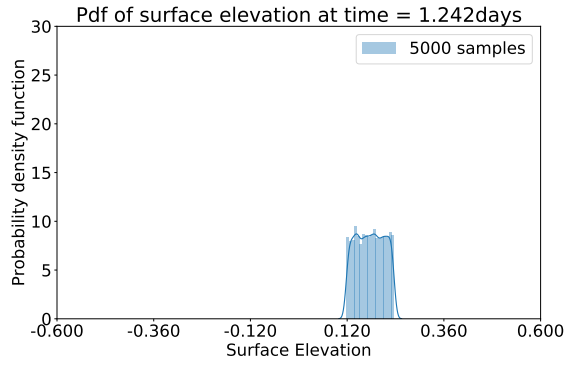
In all the cases studied in Section 4.2, three distinctive probability distributions were identified as possible candidates to represent the PDFs by properly selecting coefficients in those distributions. Clearly, different sources of uncertainty leads to differing responses of the computed PDFs. However, there are other possible distributions that can also be used to estimate the PDFs. What we have identified are possible candidates that can estimate the predicted PDFs well. The selection and study of optimal distributions is outside our current scope.



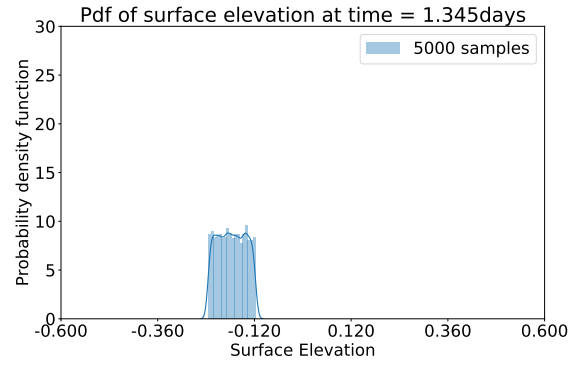
(a)



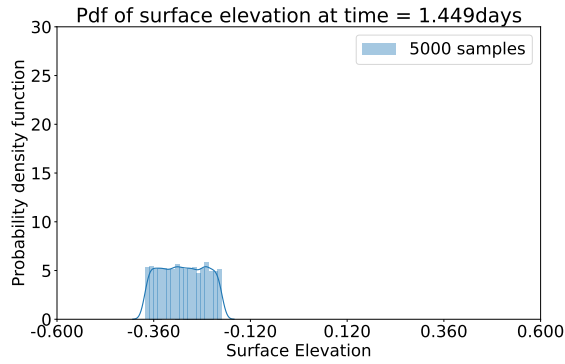
(b)



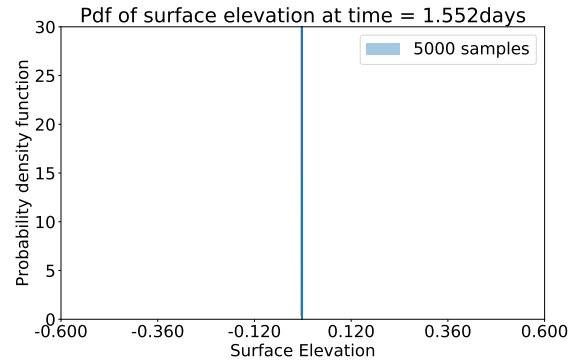
(c)



(d)



(e)

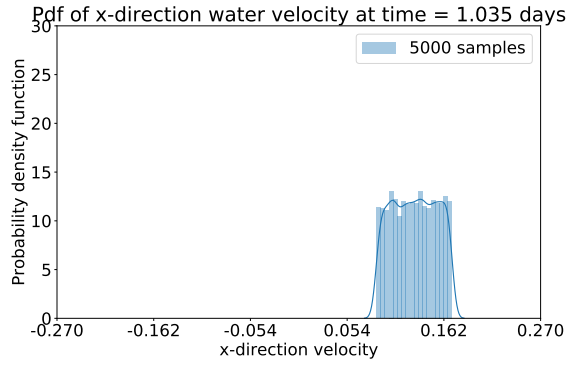


(f)

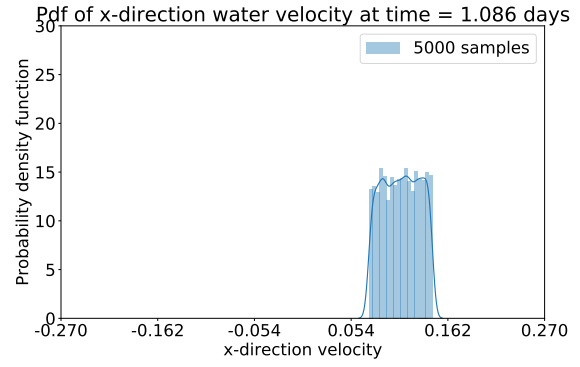
Figure 38: Uncertain boundary condition in the inlet test: The probability density of elevation at (0.0, 0.0).

4.3. The Time Varying variance field

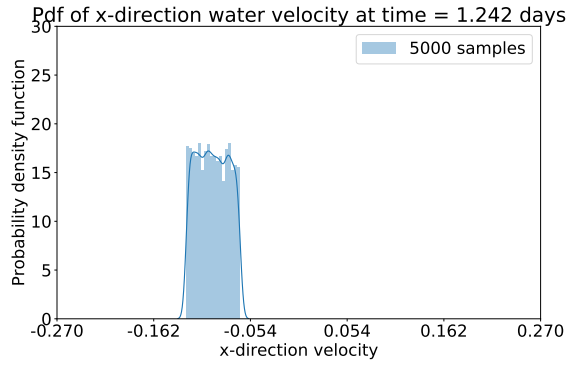
The computed surrogates from the SSWM can also be used to establish time series information on the largest uncertainty at fixed geographic locations. Alternatively, the surrogates



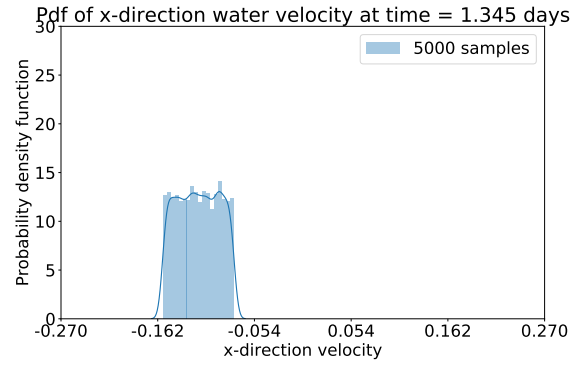
(a)



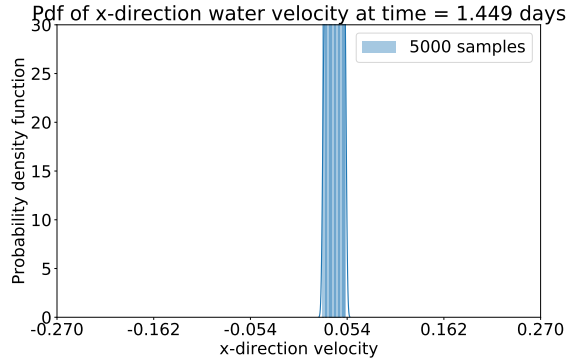
(b)



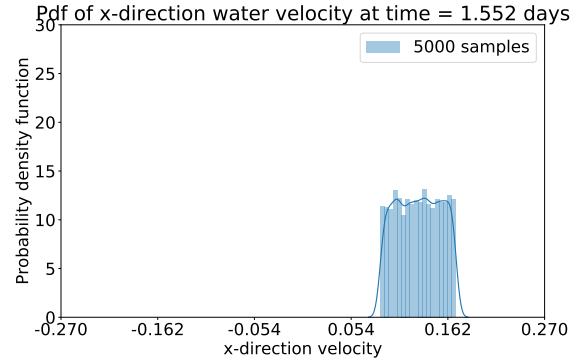
(c)



(d)



(e)



(f)

Figure 39: Uncertain boundary condition in the inlet test: The probability density of x-direction velocity at $(0.0, 0.0)$.

can do the converse at a fixed time. To investigate the maximum values of the variance as well as the relationship between it and the extreme values of the mean, we consider the

idealized inlet test case.

First, we present the mean and variance time series plots at three fixed spatial locations: $(-250.0m, 0.0m)$, $(0.0m, 0.0m)$, and $(750.0m, 0.0m)$. In Figure 40, these are plotted for both surface elevation and x component velocity. Here we observe that maximum variance occurs

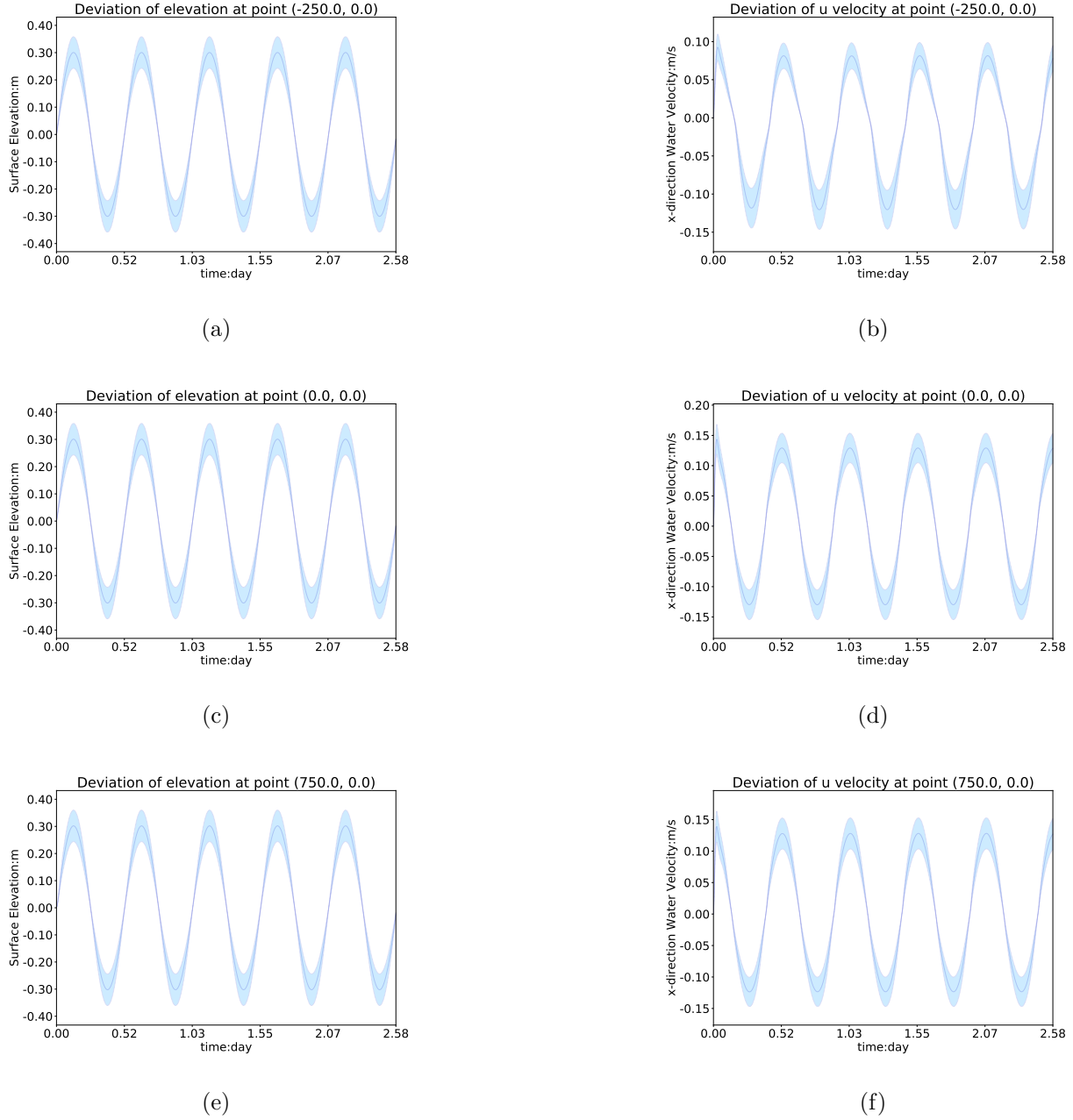


Figure 40: Mean and variance of surface elevation and x component of the velocity for the inlet test case at selected points.

at the extreme value of the mean at all points for both surface elevation and velocity. This indicates that the largest variance occurs at the extreme mean over time for both surface elevation and water velocity. Second, we consider the converse situation and explore the mean and variance at fixed times for the full domain. To this end, we select six times to show the mean and variance of the velocity magnitude over the domain, shown in Figures 41 and 42. These variances are calculated by summation of the variance in both x and y direction velocities. In these figures, we observe that the maximum variance of water velocity occurs at the extreme value of the mean field at all considered times. Further indicating that the largest variance occurs at the extreme mean over space for water velocity. In [22], an identical trend is observed for the water surface elevation for the Hurricane Ike test case. Hence, we conclude that maximum variance occurs at the extreme mean for both surface elevation and water velocity.

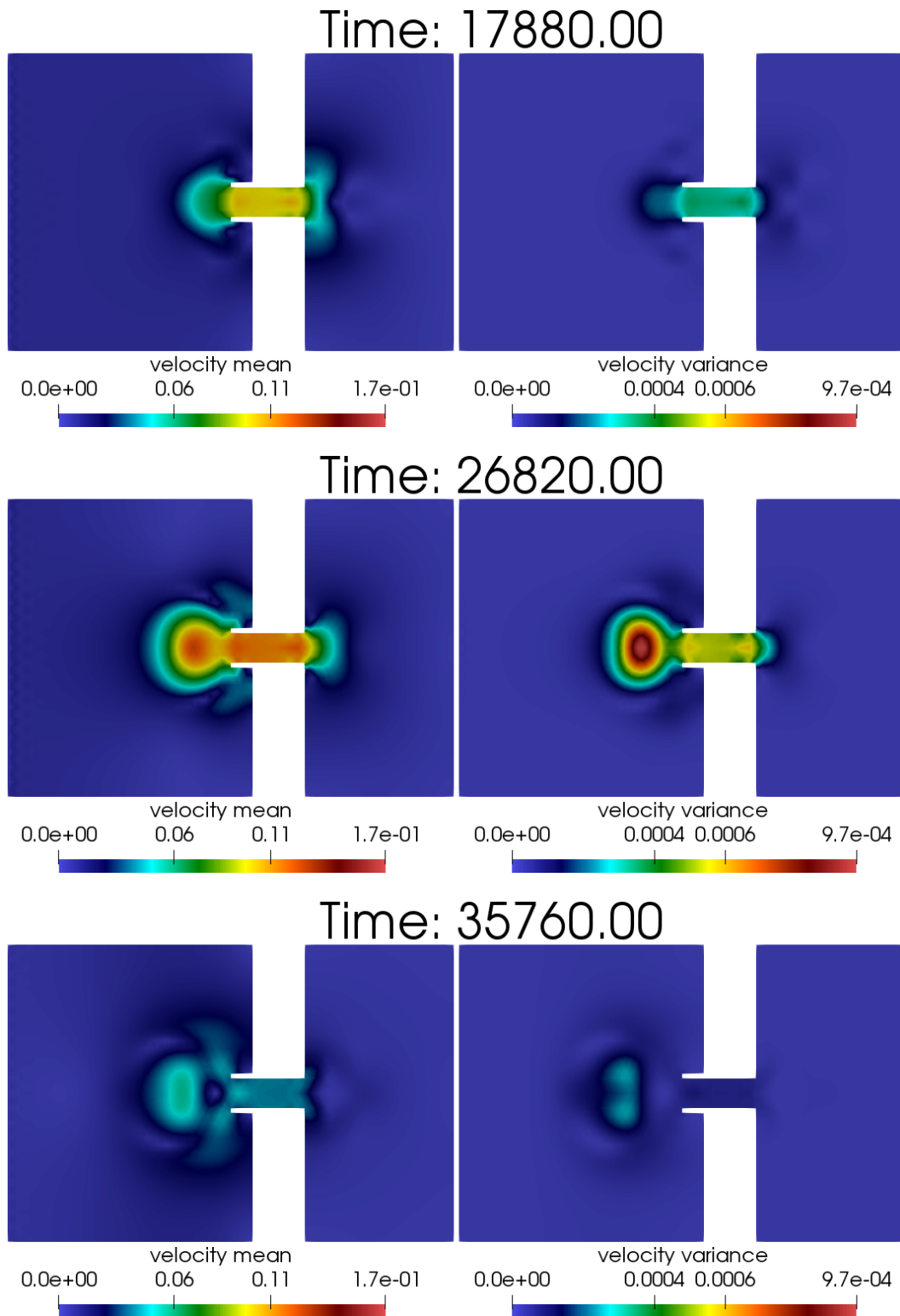


Figure 41: Mean and variance of the velocity magnitude in the inlet test case.

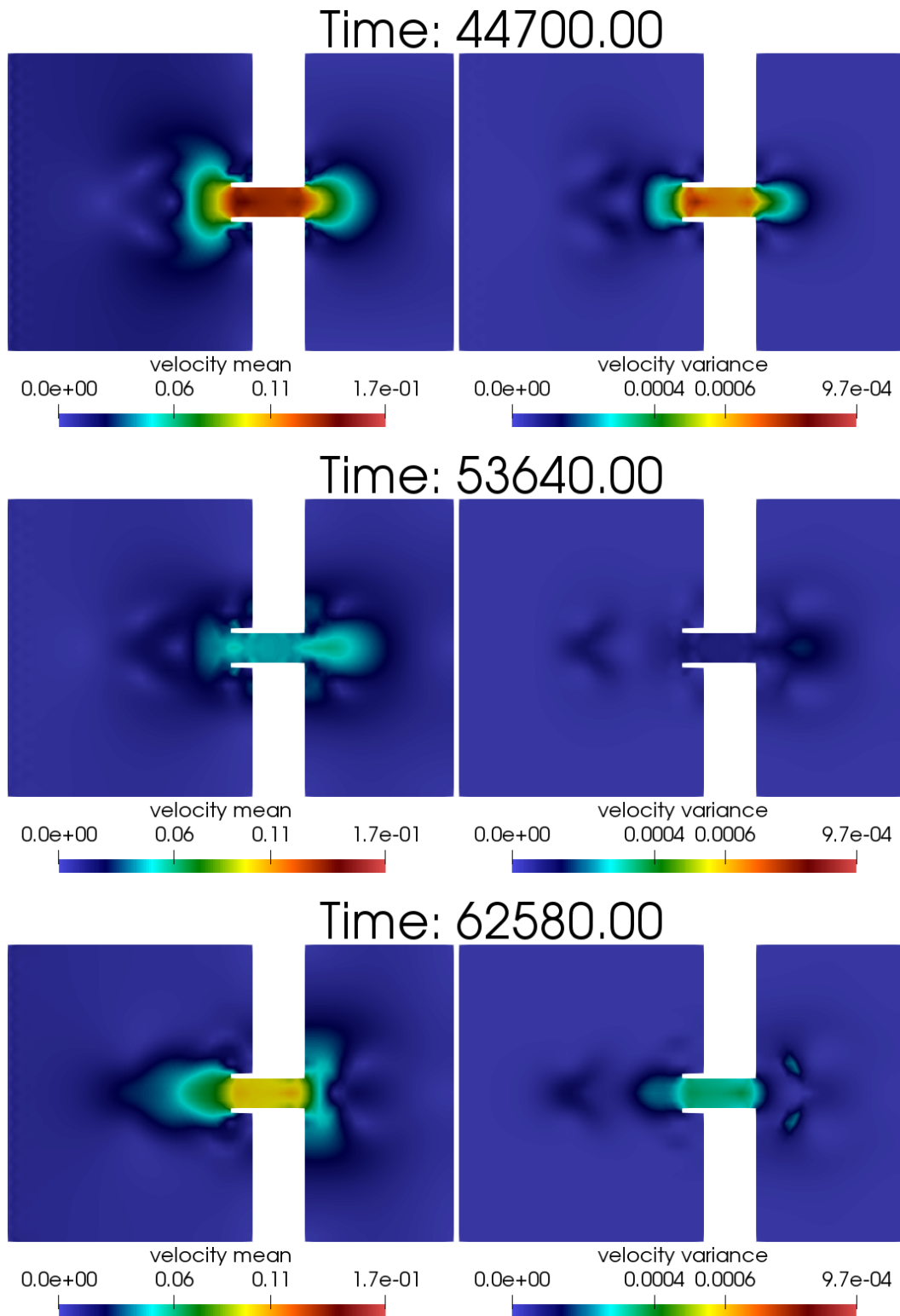


Figure 42: Mean and variance of the velocity magnitude in the inlet test case.

5. Prediction of Hurricane Storm Surge under Uncertain Wind Drag Coefficient

In this section, we use the two hurricane test cases introduced in Section 3.1.4 to show the reliability of the full stochastic model SSWM. For comparison purposes, we also apply the ADCIRC model to the same cases using identical inputs and FE meshes. The only difference between these models are the wind drag coefficients. In the SSWM it is assumed to be uncertain, with the form of $C_d = \xi_1 C_d^{Powell}$, ξ_1 uniformly distributed $\xi_1 \sim U(0.8, 1.2)$; whereas in ADCIRC it is deterministic, i.e., $C_d = C_d^{Powell}$. To present a comparison of the SSWM and the deterministic ADCIRC model, we perform three sets of numerical experiments in each of the following three sub sections. These comparisons will be performed by considering specific points on the Texas and Louisiana coasts. For the Hurricane Ike test case, we show these locations in Figure 43 and for Hurricane Harvey in Figure 44. Note that the numbering of these locations is based on the numbering of the nodes in our FE mesh.

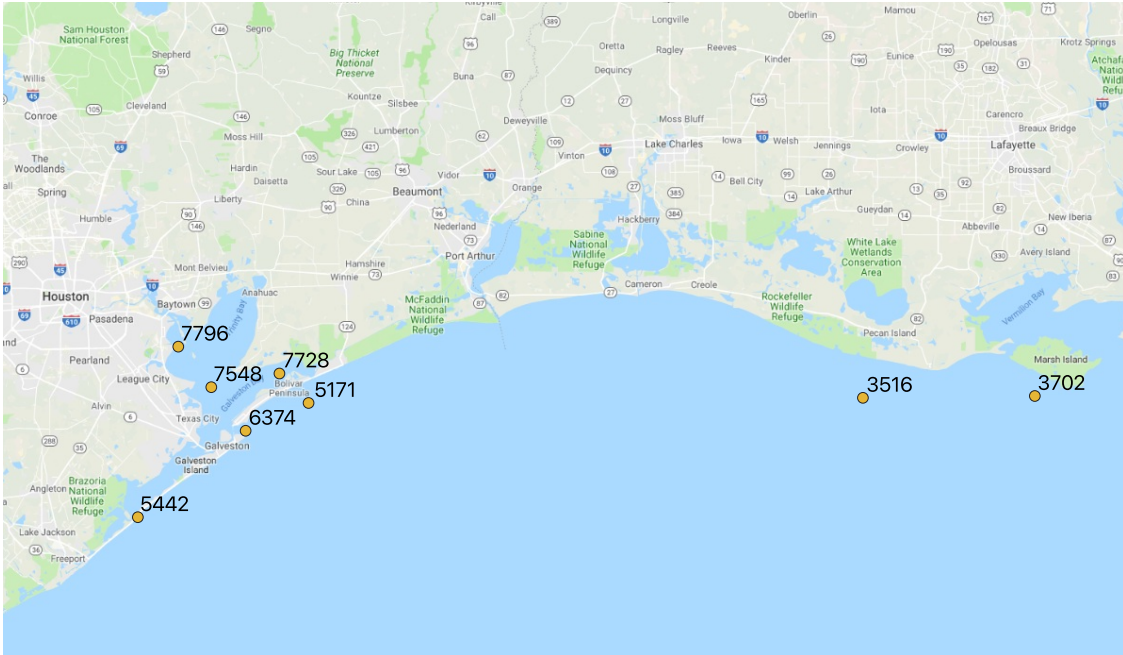


Figure 43: Spatial points for model comparison during Hurricane Ike 2008.

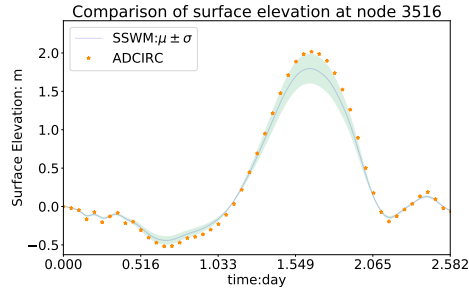
5.1. Time Series Surface Elevation Comparison

We first compare the surface elevations between ADCIRC and the SSWM at specific locations on the Texas coast. The SSWM provides a predicted PDF at each point in space

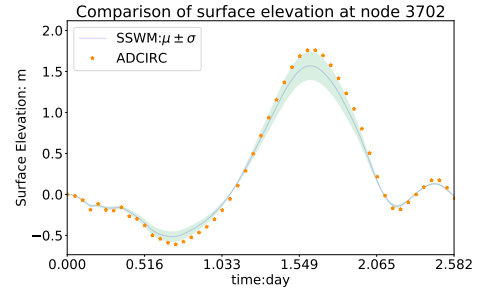


Figure 44: Spatial points for model comparison during Hurricane Harvey 2017.

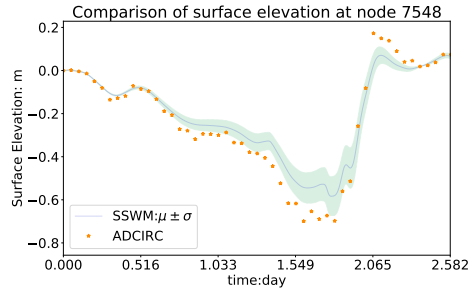
and time and we therefore visually present the mean and variance by plotting the interval $[\mu - \sigma, \mu + \sigma]$. To this end we select eight points along the coast to compare the time series surface elevation against the benchmark ADCIRC solution. The results for Hurricanes Ike and Harvey are presented in Figures 45 and 46, respectively. In these figures we observe that the SSWM mean solution agrees very well with the benchmark ADCIRC solution, which demonstrates that the trend of the predicted mean solution is reliable compared to that of ADCIRC. Note that the discrepancies seen in Figure 45(g) at node 5442 during Hurricane Ike are likely due to the strong localized effects this location experiences as it is close to a tidal inlet. Also observe the good agreement in the timing of the peak elevation for both hurricanes which is of great importance when producing forecasts. This demonstrates that the timing of the peak surge given by the predicted mean solution is reliable compared to that of ADCIRC. We also observe that the benchmark ADCIRC solution around the local peak surge falls within the green shaded area at most of the points in Figures 45 and 46. Note that the predicted range of elevation must be a superset of this interval which indicates that the predicted range also contains the benchmark ADCIRC solution. Finally, we note that the variance reaches its maximum in both troughs and crests of the time series.



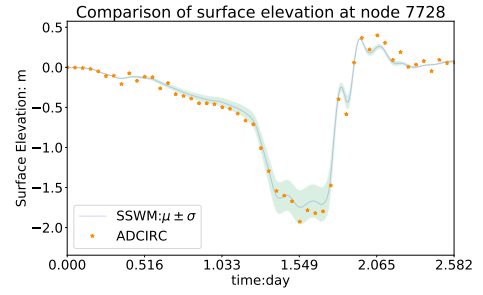
(a)



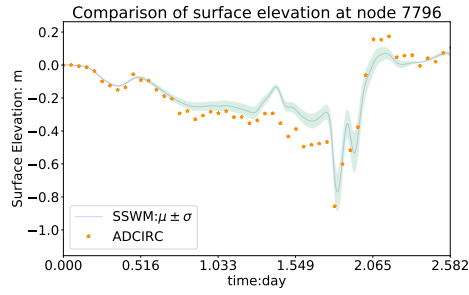
(b)



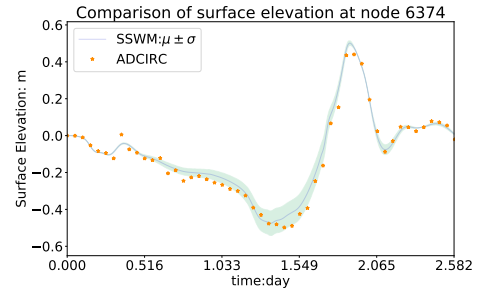
(c)



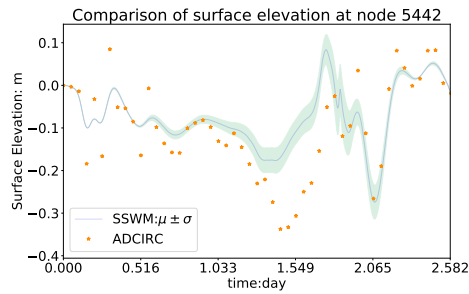
(d)



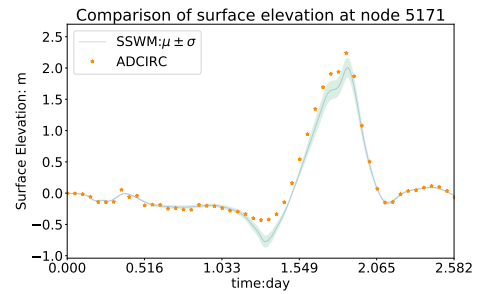
(e)



(f)



(g)



(h)

Figure 45: SSWM Surface elevation surrogate compared to deterministic ADCIRC output for Hurricane Ike.

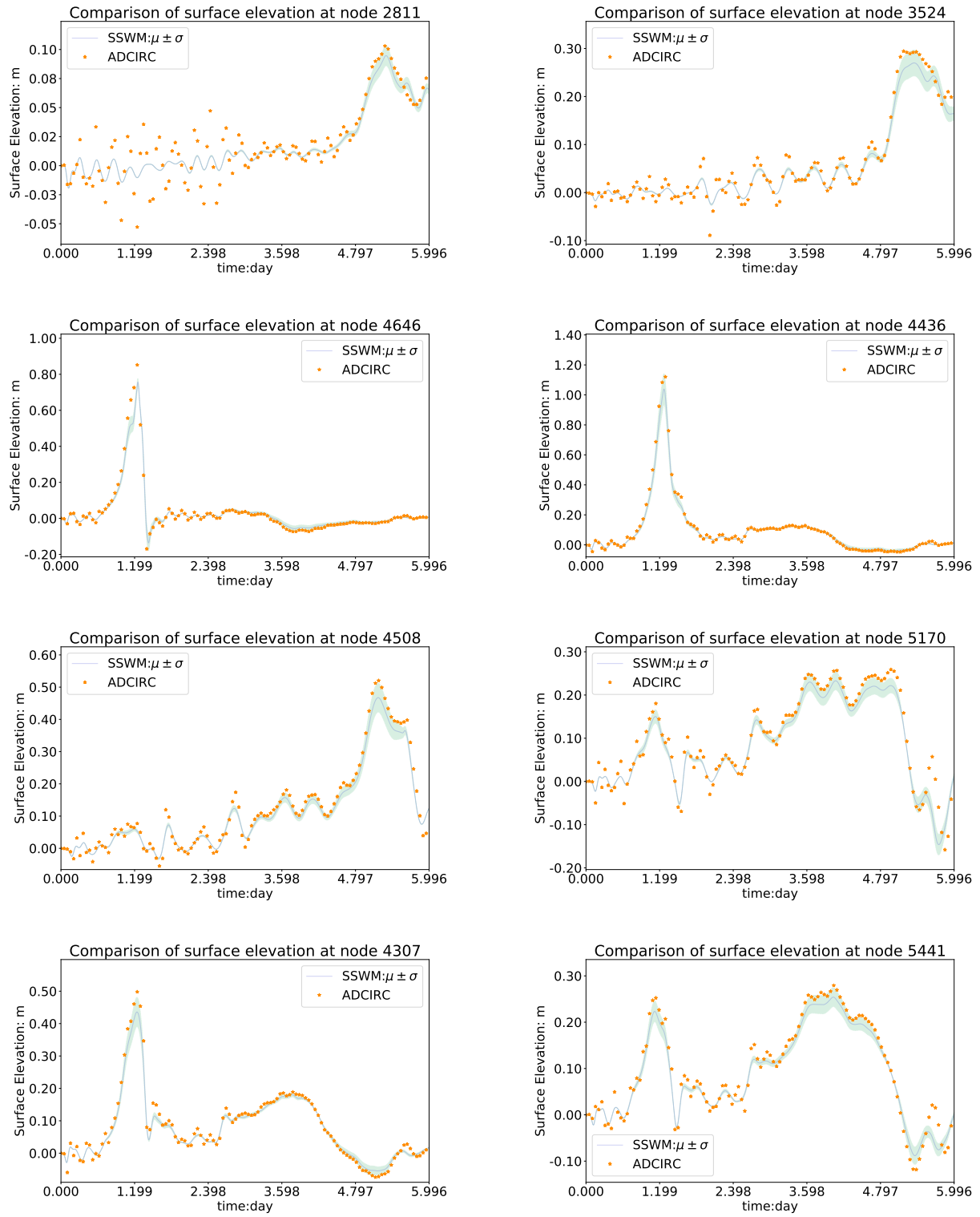


Figure 46: SSWM Surface elevation surrogate compared to deterministic ADCIRC output for Hurricane Harvey.

5.2. Comparison of the SSWM Predicted PDF and ADCIRC

As demonstrated in the previous subsection, $[\mu - \sigma, \mu + \sigma]$ produces a solution range that is reliable compared to ADCIRC. However, it cannot completely represent the statistical information (*i.e.* the predicted range or support of PDF) given by the SSWM. To further demonstrate the reliability of the SSWM, we also compare the predicted PDF at specific points on the coast against the benchmark ADCIRC solution. To plot the predicted PDF, we will use 50,000 samples for three selected spatial points in each scenario.

We first consider the Hurricane Ike case and select three points in locations that underwent significant surge, *i.e.*, 3702, 3516 and 5171 (see Figure 43). In Figures 47, 48, and 49, we present the predicted PDFs, the ADCIRC solution, the 50,000 samples, and the kernel estimated PDF, *i.e.*, the Kernel Density Estimate (KDE). For Hurricane Harvey, we repeat this exercise for the points 4436, 6027, and 2811 (see Figure 44) and present the results in Figures 50, 51, and 52.

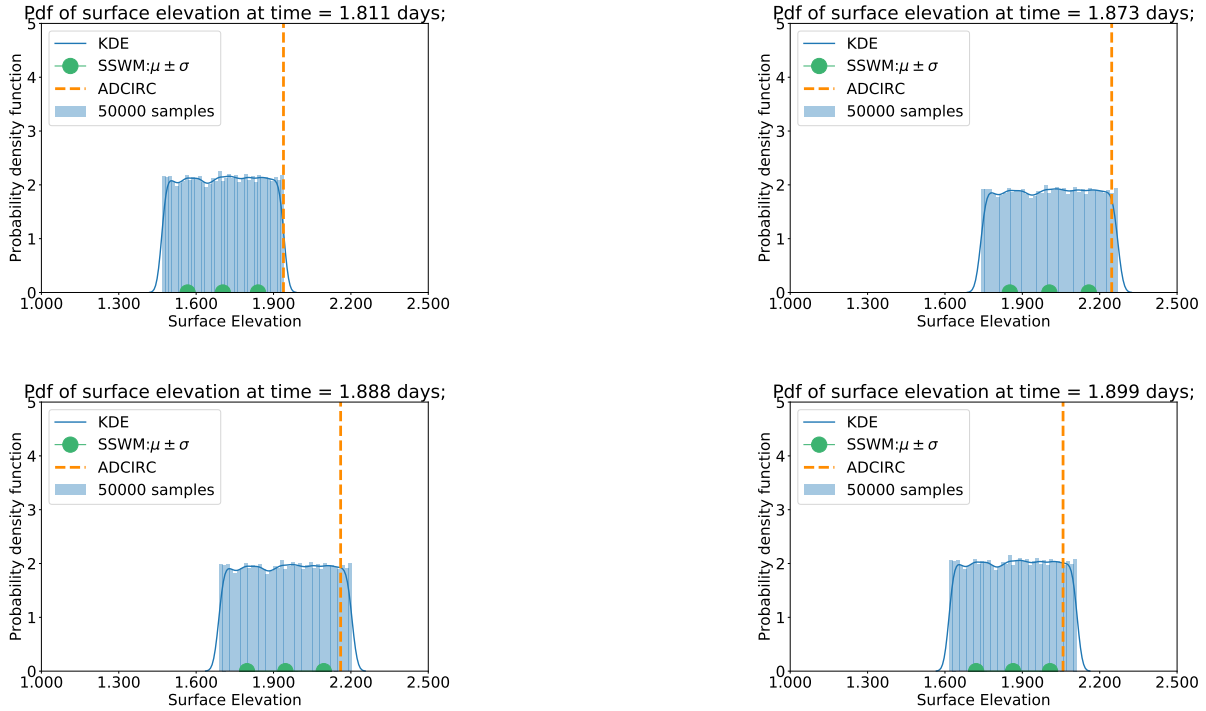


Figure 47: Predicted PDF of surface elevation compared to ADCIRC at point 5171 during Hurricane Ike.

As shown in these figures, the PDFs for surface elevation during the hurricanes resembles uniform distributions. Hence, for each point, the SSWM provides a predicted range (*i.e.*, the

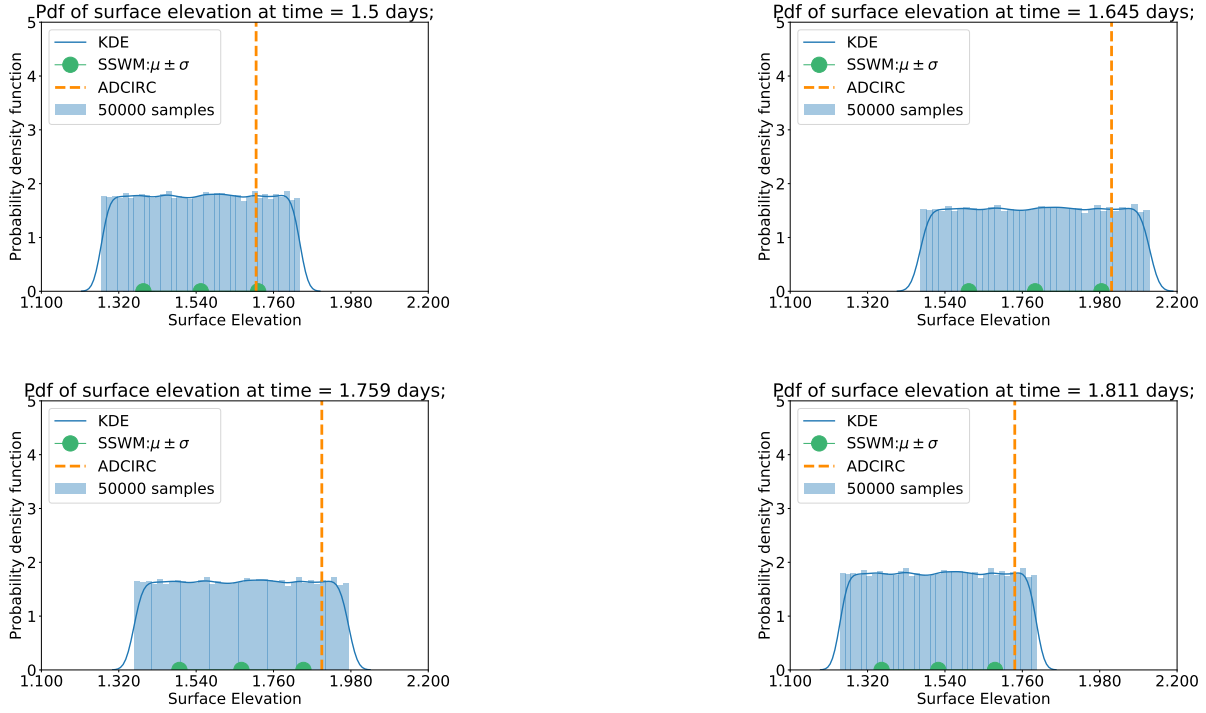


Figure 48: Predicted PDF of surface elevation compared to ADCIRC at point 3516 during Hurricane Ike.

interval covered by the blue histogram at the horizontal axis) within which the values have an almost equal chance of occurrence. We also observe that in most cases the benchmark ADCIRC solution is within the predicted range. In other words, given a range for the uncertain input C_d , the SSWM is able to provide a predicted range that includes the benchmark solution. Inspection of the results in Figures 47 through 52, leads to the observation that the widest predicted range (1.45m to 2.11m) across the two scenarios is found in Figure 48(b). This means that, with an offset from the true wind drag coefficient by scaling the truth 0.8 to 1.2 times (i.e., $C_d = \xi_1 C_d^{truth, ADCIRC}$, with $\xi_1 \sim U[0.8, 1.2]$) we expect that the peak surge will be offset from the truth by 0.66m. This further implies that the peak surge value is very sensitive to the wind drag coefficient, which is in fact a well known phenomenon that is critical in the calibration and validation of ADCIRC models.

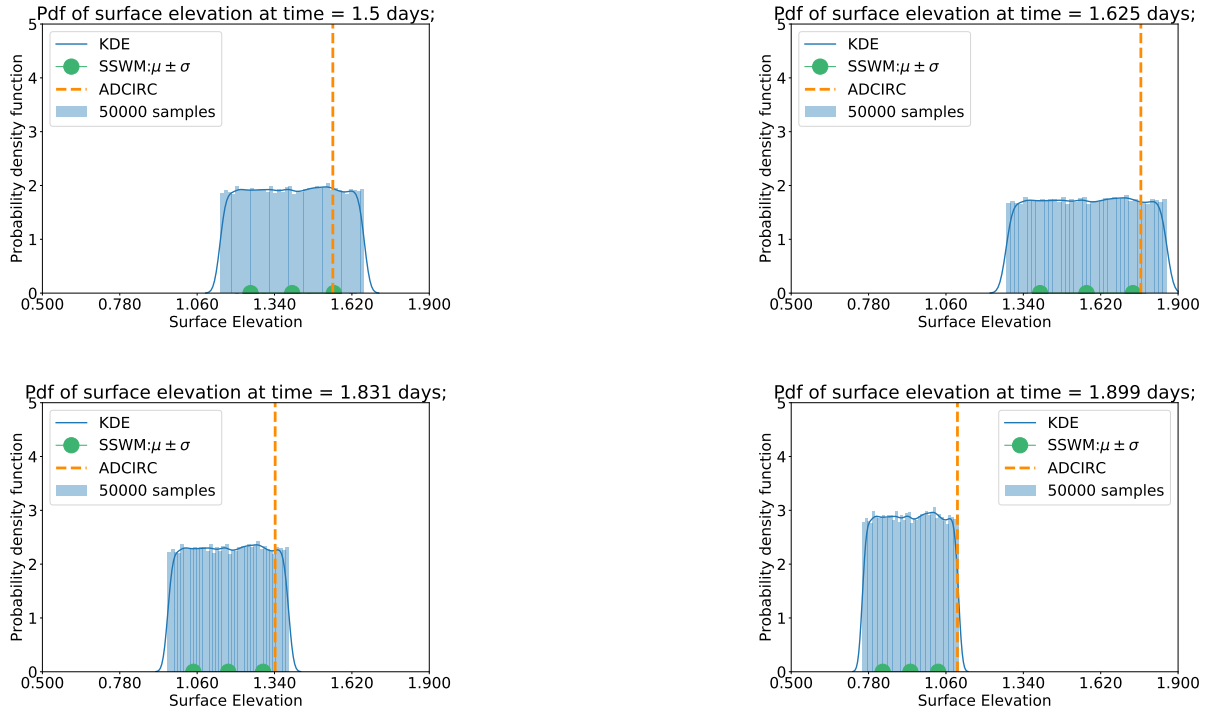


Figure 49: Predicted PDF of surface elevation compared to ADCIRC at point 3702 during Hurricane Ike.

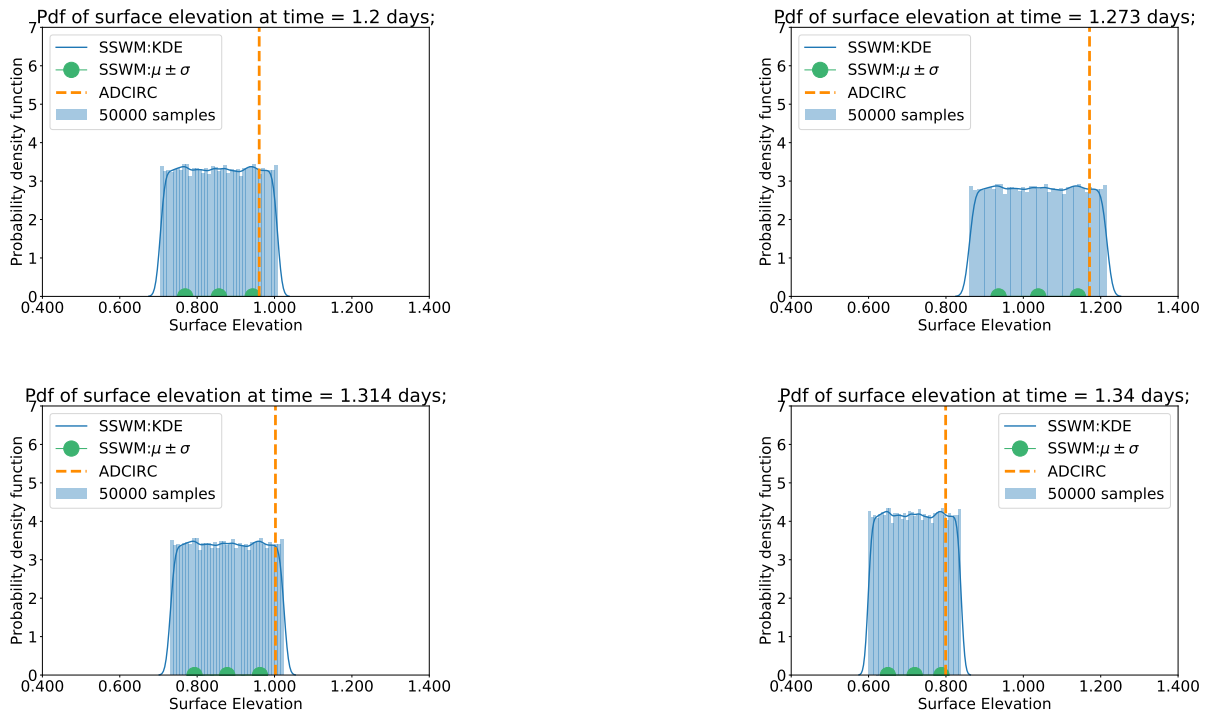


Figure 50: Predicted PDF of surface elevation compared to ADCIRC at point 4436 during Hurricane Harvey.

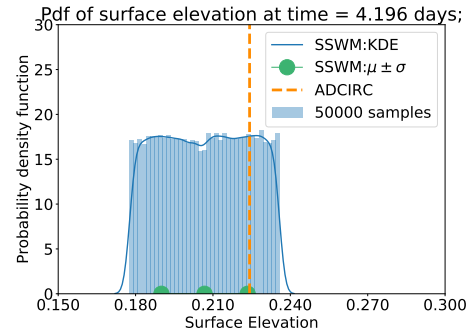
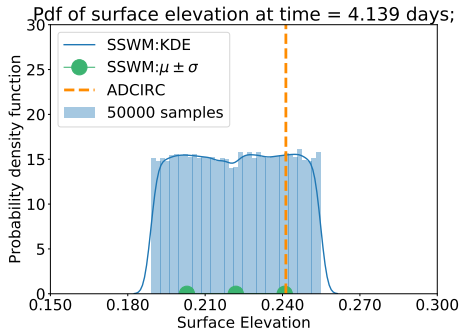
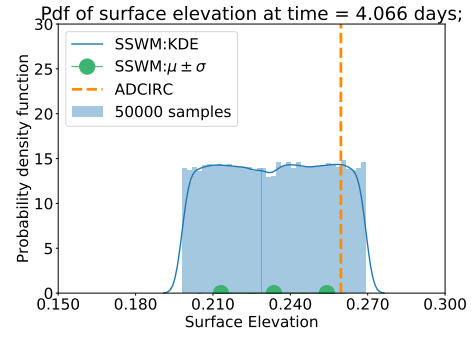
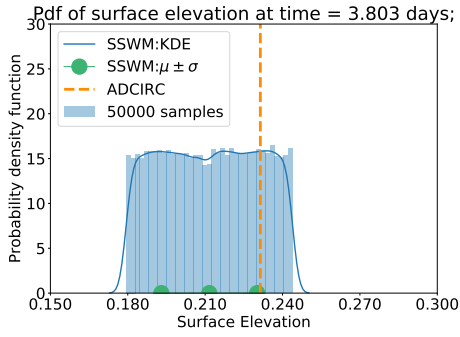


Figure 51: Predicted PDF of surface elevation compared to ADCIRC at point 6027 during Hurricane Harvey.

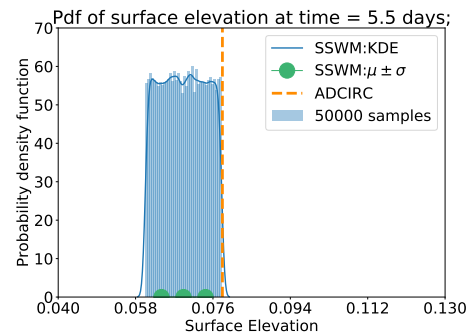
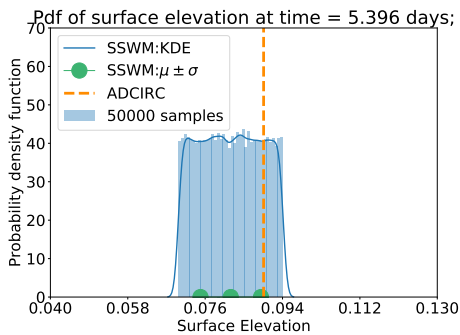
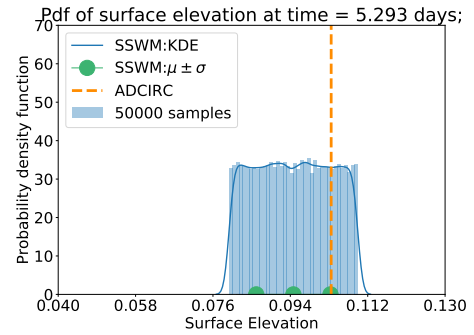
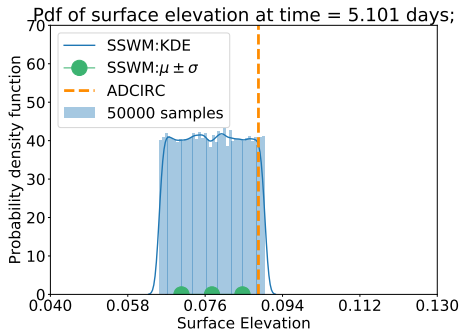


Figure 52: Predicted PDF of surface elevation compared to ADCIRC at point 2811 during Hurricane Harvey.

5.3. Maximum Surface Elevation Comparison

In an operational storm surge prediction system, it is computationally intractable to draw a predicted PDF at each point and time. Thus, to predict surge in real-time when a hurricane is forecast under uncertain wind drag coefficients, a reliable predictor from the SSWM is needed. Therefore, we propose a predictor from the SSWM and demonstrate its effectiveness at predicting the maximum surface elevation under the consideration of an uncertain wind drag coefficient. Here, we propose a safe predictor $\mu + \sigma$, for the purpose of real-time prediction under the situation of an uncertain wind drag coefficient.

To show the effectiveness of the proposed predictor $\mu + \sigma$, we select 23 and 30 spatial points for Hurricane Ike and Harvey, respectively. In Figures 53 and 54, we present the comparison of the maximum surface elevation between ADCIRC and the SSWM proposed predictor.

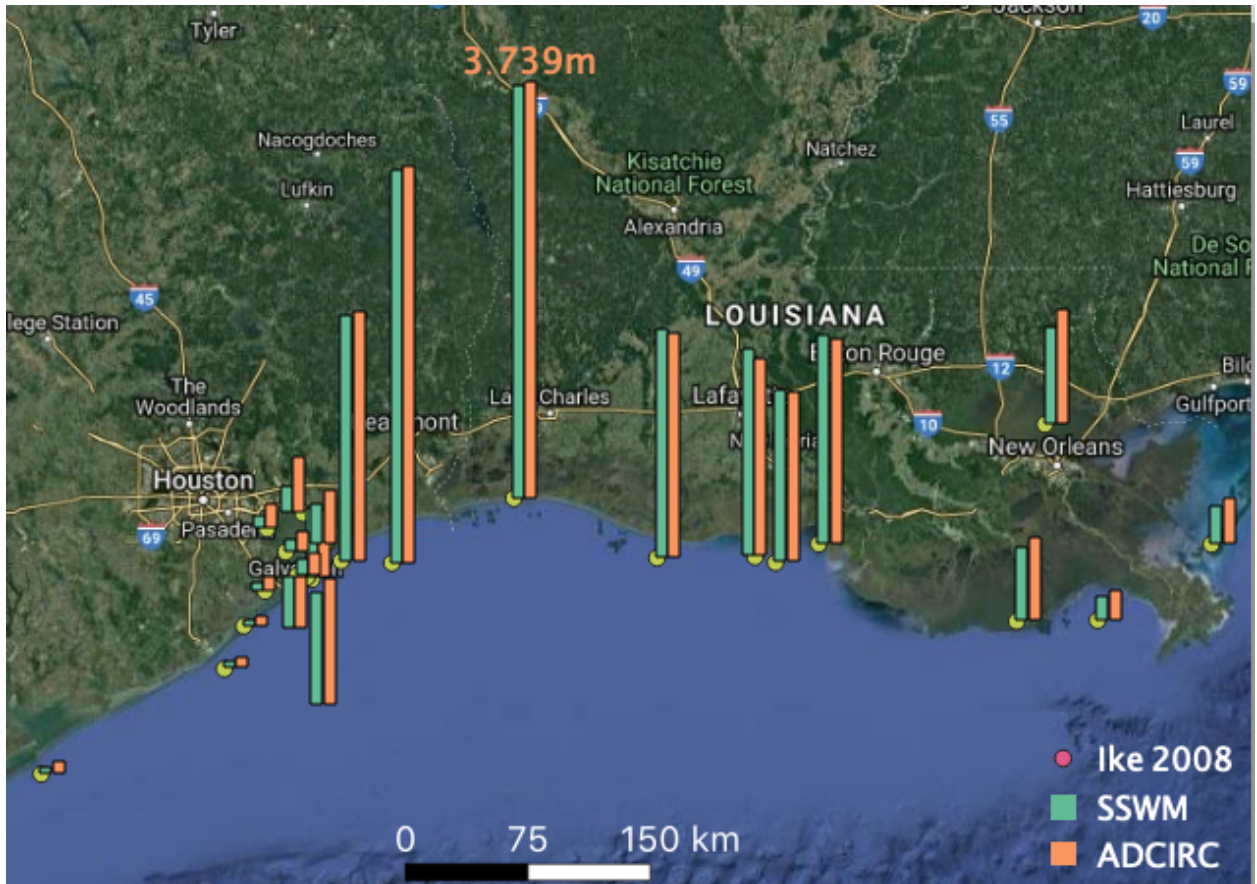


Figure 53: Maximum surface elevation comparison between ADCIRC and SSWM for Hurricane Ike.

These results show that the proposed indicator $\mu + \sigma$ underestimates the maximum surface

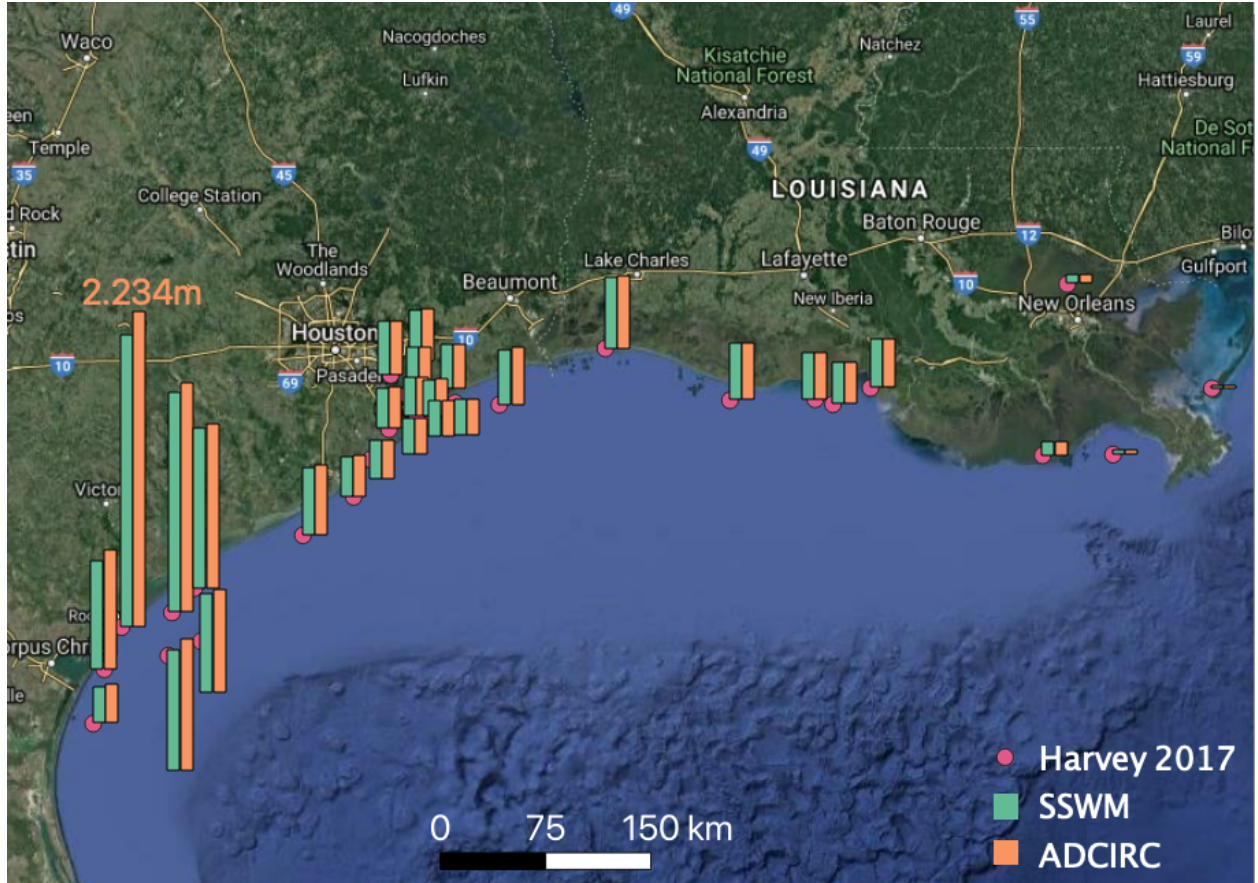


Figure 54: Maximum surface elevation comparison between ADCIRC and SSWM for Hurricane Harvey.

elevation inside the Galveston Bay area for Hurricane Ike. This underestimation is also apparent along the western coast of Texas for Hurricane Harvey. Otherwise, close agreement is observed in both cases. This suggests that the proposed predictor $\mu + \sigma$ given by the SSWM is reliable for real-time prediction of maximum surface elevation, under the present condition of a uniformly distributed uncertain wind drag coefficient.

5.4. Notes on the Visualization and Analysis of the SSWM Outputs

Based on the statistical analysis and visual representations in this section, we draw multiple conclusions: *i)* the variance in the model outputs increases as the variances in the model inputs increase, *ii)* we show that the maximum variance occurs at the extreme mean for both surface elevation and water velocity over space and over time, and *iii)* we have explored the pattern of the distributions given by the surrogate at different locations and different time. We noticed strong similarity between the predicted probability density

functions between the output quantities, over space and time in each test case. We also show that the types of predicted probability density functions varies under different uncertain sources. For the two considered hurricanes, we further showed the reliability of the SSWM and proposed a reliable predictor for the SSWM to use in real-time by considering mean outputs as well as predicted PDFs.

6. Concluding Remarks

In this paper, we have developed and extensively verified a stabilized stochastic shallow water model, i.e., the SSWM and conducted a comprehensive statistical analysis on the resulting SSWM surrogate outputs. We have also conducted a validation exercise for hindcasting of two past hurricanes, Ike and Harvey. We also propose a safe and reliable predictor $\mu + \sigma$ to show that the SSWM can be used for real-time predictions during hurricanes. The effectivity of the predictor is demonstrated through hindcasting of maximum surge in Hurricane Ike and Harvey, respectively.

It is our hope that this SSWM can be used to enhance the reliability of current state-of-the-art hurricane storm surge prediction systems. For future works, we note there is gap in theory regarding the stability of a stochastic hyperbolic system. And, although we have provided one approach to stabilize such a system, different stabilization techniques are still needed for solving multiscale problems under more extreme conditions, such as wetting and drying of elements. Additionally, while the uniformly distributed uncertain input lead to uncertain outputs of other distributions, a natural question of how to determine the output distribution before running the stochastic model arises. This opens a new field of studying the internal mechanism in the relationship between input distribution and output distribution.

Acknowledgements

The authors would like to gratefully acknowledge the use of the "ADCIRC" allocation at the Texas Advanced Computing Center at the University of Texas at Austin. This work has been supported by the United States National Science Foundation - NSF PREEVENTS Track 2 Program, under NSF Grant Number 1855047

References

- [1] H. N. Najm, Uncertainty quantification and polynomial chaos techniques in computational fluid dynamics, *Annual review of fluid mechanics* 41 (2009) 35–52.
- [2] I. R. Calder, A stochastic model of rainfall interception, *Journal of Hydrology* 89 (1-2) (1986) 65–71.
- [3] I. Rodriguez-Iturbe, D. R. Cox, V. Isham, Some models for rainfall based on stochastic point processes, *Proceedings of the Royal Society of London. A. Mathematical and Physical Sciences* 410 (1839) (1987) 269–288.
- [4] J. Huh, A. Haldar, Stochastic finite-element-based seismic risk of nonlinear structures, *Journal of structural engineering* 127 (3) (2001) 323–329.
- [5] D. M. Ghiocel, R. G. Ghanem, Stochastic finite-element analysis of seismic soil–structure interaction, *Journal of Engineering Mechanics* 128 (1) (2002) 66–77.
- [6] X. Guo, D. Dias, C. Carvajal, L. Peyras, P. Breul, Reliability analysis of embankment dam sliding stability using the sparse polynomial chaos expansion, *Engineering Structures* 174 (2018) 295–307.
- [7] M. Rajabalinejad, T. Mahdi, P. van Gelder, Stochastic methods for safety assessment of the flood defense system in the scheldt estuary of the Netherlands, *Natural hazards* 55 (1) (2010) 123–144.
- [8] P. Sochala, C. Chen, C. Dawson, M. Iskandarani, A polynomial chaos framework for probabilistic predictions of storm surge events, *Computational Geosciences* 24 (1) (2020) 109–128.
- [9] N. Metropolis, S. Ulam, The Monte Carlo method, *Journal of the American statistical association* 44 (247) (1949) 335–341.
- [10] B. Minasny, A. B. McBratney, A conditioned Latin hypercube method for sampling in the presence of ancillary information, *Computers & geosciences* 32 (9) (2006) 1378–1388.

- [11] L. Chamoin, P. Ladevèze, A non-intrusive method for the calculation of strict and efficient bounds of calculated outputs of interest in linear viscoelasticity problems, *Computer Methods in Applied Mechanics and Engineering* 197 (9-12) (2008) 994–1014.
- [12] X. Wan, G. E. Karniadakis, Multi-element generalized polynomial chaos for arbitrary probability measures, *SIAM Journal on Scientific Computing* 28 (3) (2006) 901–928.
- [13] L. W.-T. Ng, M. Eldred, Multifidelity uncertainty quantification using non-intrusive polynomial chaos and stochastic collocation, in: 53rd AIAA/ASME/ASCE/AHS/ASC Structures, Structural Dynamics and Materials Conference 20th AIAA/ASME/AHS Adaptive Structures Conference 14th AIAA, 2012, p. 1852.
- [14] M. Eldred, Recent advances in non-intrusive polynomial chaos and stochastic collocation methods for uncertainty analysis and design, in: 50th AIAA/ASME/ASCE/AHS/ASC Structures, Structural Dynamics, and Materials Conference 17th AIAA/ASME/AHS Adaptive Structures Conference 11th AIAA No, 2009, p. 2274.
- [15] M. Hadigol, A. Doostan, Least squares polynomial chaos expansion: A review of sampling strategies, *Computer Methods in Applied Mechanics and Engineering* 332 (2018) 382–407.
- [16] J. Hu, S. Chen, A. Behrangi, H. Yuan, Parametric uncertainty assessment in hydrological modeling using the generalized polynomial chaos expansion, *Journal of Hydrology* 579 (2019) 124158.
- [17] D. Xiu, *Numerical methods for stochastic computations: a spectral method approach*, Princeton university press, 2010.
- [18] P. E. Farrell, D. A. Ham, S. W. Funke, M. E. Rognes, Automated derivation of the adjoint of high-level transient finite element programs, *SIAM Journal on Scientific Computing* 35 (4) (2013) C369–C393.
- [19] S. W. Funke, P. E. Farrell, M. Piggott, Tidal turbine array optimisation using the adjoint approach, *Renewable Energy* 63 (2014) 658–673.

- [20] K. Goda, A multistep technique with implicit difference schemes for calculating two-or three-dimensional cavity flows, *Journal of computational physics* 30 (1) (1979) 76–95.
- [21] J. Simo, F. Armero, Unconditional stability and long-term behavior of transient algorithms for the incompressible Navier-Stokes and Euler equations, *Computer Methods in Applied Mechanics and Engineering* 111 (1-2) (1994) 111–154.
- [22] C. Chen, Intrusive polynomial chaos uncertainty quantification on shallow water system, Ph.D. thesis, The University of Texas at Austin (2020).
- [23] A. N. Brooks, T. J. Hughes, Streamline upwind/Petrov-Galerkin formulations for convection dominated flows with particular emphasis on the incompressible Navier-Stokes equations, *Computer methods in applied mechanics and engineering* 32 (1-3) (1982) 199–259.
- [24] T. E. Tezduyar, Computation of moving boundaries and interfaces and stabilization parameters, *International Journal for Numerical Methods in Fluids* 43 (5) (2003) 555–575.
- [25] T. E. Tezduyar, Stabilization parameters and element length scales in SUPG and PSPG formulations, in: *Book of Abstracts of An Euro Conference on Numerical Methods and Computational Mechanics*, Miskolc, Hungary, 2002.
- [26] T. J. Hughes, M. Mallet, M. Akira, A new finite element formulation for computational fluid dynamics: II. Beyond SUPG, *Computer methods in applied mechanics and engineering* 54 (3) (1986) 341–355.
- [27] E. Burman, M. A. Fernández, Continuous interior penalty finite element method for the time-dependent navier–stokes equations: space discretization and convergence, *Numerische Mathematik* 107 (1) (2007) 39–77.
- [28] A. Logg, K.-A. Mardal, G. Wells, Automated solution of differential equations by the finite element method: The FEniCS book, Vol. 84, Springer Science & Business Media, 2012.

- [29] A. Logg, G. N. Wells, Dofin: Automated finite element computing, *ACM Transactions on Mathematical Software (TOMS)* 37 (2) (2010) 20.
- [30] R. C. Kirby, A. Logg, A compiler for variational forms, *ACM Transactions on Mathematical Software (TOMS)* 32 (3) (2006) 417–444.
- [31] M. S. Alnæs, A. Logg, K. B. Ølgaard, M. E. Rognes, G. N. Wells, Unified form language: A domain-specific language for weak formulations of partial differential equations, *ACM Transactions on Mathematical Software (TOMS)* 40 (2) (2014) 9.
- [32] M. S. Alnæs, A. Logg, K.-A. Mardal, O. Skavhaug, H. P. Langtangen, Unified framework for finite element assembly, *International Journal of Computational Science and Engineering* 4 (4) (2009) 231–244.
- [33] R. C. Kirby, Algorithm 839: Fiat, a new paradigm for computing finite element basis functions, *ACM Transactions on Mathematical Software (TOMS)* 30 (4) (2004) 502–516.
- [34] J. Feinberg, H. P. Langtangen, Chaospy: An open source tool for designing methods of uncertainty quantification, *Journal of Computational Science* 11 (2015) 46–57.
- [35] E. J. Kubatko, J. J. Westerink, C. Dawson, hp discontinuous galerkin methods for advection dominated problems in shallow water flow, *Computer Methods in Applied Mechanics and Engineering* 196 (1-3) (2006) 437–451.
- [36] M. D. Powell, P. J. Vickery, T. A. Reinhold, Reduced drag coefficient for high wind speeds in tropical cyclones, *Nature* 422 (6929) (2003) 279.
- [37] K. M. Bryant, M. Akbar, An exploration of wind stress calculation techniques in hurricane storm surge modeling, *Journal of Marine Science and Engineering* 4 (3) (2016).
doi:10.3390/jmse4030058.
URL <https://www.mdpi.com/2077-1312/4/3/58>
- [38] R. A. Luetich, J. J. Westerink, N. W. Scheffner, et al., ADCIRC: an advanced three-dimensional circulation model for shelves, coasts, and estuaries. Report 1, theory and methodology of ADCIRC-2DD1 and ADCIRC-3DL (1992).

- [39] W. J. Pringle, D. Wirasaet, K. J. Roberts, J. J. Westerink, Global storm tide modeling with ADCIRC v55: Unstructured mesh design and performance, *Geoscientific Model Development Discussions* 2020 (2020) 1–30. doi:10.5194/gmd-2020-123.
URL <https://gmd.copernicus.org/preprints/gmd-2020-123/>
- [40] C. Trahan, G. Savant, R. Berger, M. Farthing, T. McAlpin, L. Pettey, G. Choudhary, C. N. Dawson, Formulation and application of the adaptive hydraulics three-dimensional shallow water and transport models, *Journal of Computational Physics* 374 (2018) 47–90.
- [41] S. S. Wang, P. J. Roache, R. A. Schmalz, Y. Jia, P. E. Smith, Verification and validation of 3d free-surface flow models, American Society of Civil Engineers, 2009.
- [42] NOAA tides and currents station database, <https://tidesandcurrents.noaa.gov/>.
- [43] R. A. Luetich Jr, J. J. Westerink, A solution for the vertical variation of stress, rather than velocity, in a three-dimensional circulation model, *International Journal for Numerical Methods in Fluids* 12 (10) (1991) 911–928.
- [44] N. Agarwal, N. R. Aluru, A domain adaptive stochastic collocation approach for analysis of mems under uncertainties, *Journal of Computational Physics* 228 (20) (2009) 7662–7688.